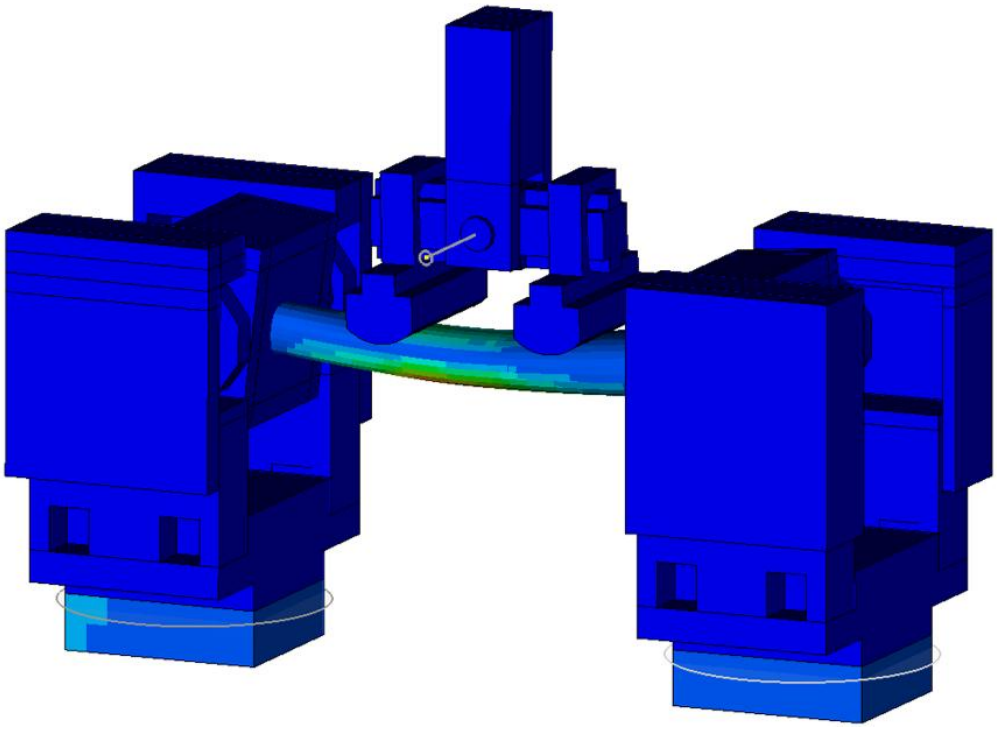

Pedestrian Lower Extremity Fracture Prediction

Development and validation of strain based Injury Risk Functions for Femur and Tibia

Master's thesis in Applied Mechanics and Mobility Engineering

Sankalp Prabhu
Chirag Suresh Kumar

Department of Mechanics and Maritime Sciences
CHALMERS UNIVERSITY OF TECHNOLOGY
Gothenburg, Sweden 2026
www.chalmers.se

Master's thesis 2026

Pedestrian Lower Extremity Fracture Prediction

Development and validation of strain based Injury Risk Function for Femur and Tibia

Sankalp Prabhu
Chirag Suresh Kumar

CHALMERS
UNIVERSITY OF TECHNOLOGY

Department of Mechanics and Maritime Sciences
Chalmers University of Technology
Gothenburg, Sweden 2026

Pedestrian Lower Extremity Fracture Prediction
Development and validation of strain based Injury Risk Function for Femur and Tibia
Sankalp Prabhu & Chirag Suresh Kumar

Supervisor: Bengt Pipkorn, Volvo Cars & Mohankumar Jayathirtha, Autoliv AB
Examiner: Johan Iraeus, Department of Mechanical Engineering

Master's Thesis 2026
Department of Mechanics and Maritime Sciences
Division of Vehicle Safety
Chalmers University of Technology
SE-412 96 Gothenburg
Telephone +46 31 772 1000

Cover: Maximum Principal Strain fringe plot for tibia four point bending FEM setup

Typeset in LaTeX
Printed by Chalmers Reproservice
Gothenburg, Sweden 2026

Pedestrian Lower Extremity Fracture Prediction
Development and validation of strain based Injury Risk Function for Femur and Tibia
Sankalp Prabhu & Chirag Suresh Kumar
Department of Mechanics and Maritime Sciences
Chalmers University of Technology

Abstract

Road traffic accidents remain a leading cause of death and serious injury globally, with vulnerable road users including pedestrians accounting for a disproportionate share of the fatalities. In pedestrian-vehicle collisions, the lower extremities are among the most frequently injured body regions, with fractures of the femoral and tibial shafts representing major injury outcomes. While finite element based human body models are widely used in automotive safety research, their pedestrian injury assessment capabilities are limited by the absence of validated fracture risk functions for the lower extremity long bones.

This thesis addresses this gap by developing and validating age dependent, strain based injury functions for femoral and tibial shafts for the SAFER HBM. Probabilistic Weibull survival models were fitted to cortical bone coupon test data using a Monte Carlo reconstruction framework that accounts for the uncertainty associated with the use of aggregated experimental data. The resulting injury risk functions express fracture probability as a function of maximum principal strain and age.

Component level finite element simulations of isolated femur three point bending and tibia four point bending experiments were conducted to validate the developed framework. The predicted force from the femur model was in agreement with the test results. The femur injury risk functions predicted fracture probability above 50% for four of the eight fracturing specimen, providing validation of the framework. The tibia simulations showed variable force time agreement, and the extracted cortical strain at the time of experimental peak force were clustered in the range of 1% to 1.7% across all tibia specimen which was below the fracture threshold. This outcome is however attributed to the highly dynamic nature of the experimental setup, where direct impactor contact without a foam padding introduced loading conditions that the current modeling framework could not fully replicate.

The developed injury risk functions represent a first step toward biofidelic pedestrian fracture assessment with SAFER HBM, with the femur IRF considered suitable for use and tibia IRF providing reasonable first estimate pending improved experimental validation.

Keywords: Pedestrian Safety, Human Body Model, SAFER HBM, Femur, Tibia, Injury Risk Function, Weibull Survival Analysis, Finite Element Method.

Acknowledgements

We would like to express our sincere gratitude to the individuals and organisations who supported and guided us throughout this thesis. At Volvo Cars, we are grateful to Bengt Pipkorn for his supervision and to Linus Wågström and Jonas Östh for their mentorship and continuous support during the course of this work. From Chalmers University of Technology, we would like to thank our examiner Johan Iraeus for his valuable feedback and encouragement throughout the project. At Autoliv, we extend our appreciation to Mohankumar Jayathirtha for his supervision and the direction he provided, which was instrumental in shaping the scope of this thesis. We also thank Dynamore for providing us with training in LS-DYNA, which was essential to the technical work carried out in this project. Finally, we are grateful to Junior Noss from the University of Virginia for his generous support and for sharing data from previous experiments.

Sankalp Prabhu & Chirag Kumar, Gothenburg, June 2026

List of Acronyms

Below is the list of acronyms that have been used throughout this thesis listed in alphabetical order:

AFT	Accelerated Failure Time
AIC	Akaike Information Criterion
ATD	Anthropometric Test Device
CI	Confidence Interval
FE	Finite Element
FEM	Finite Element Method
HBM	Human Body Model
IRF	Injury Risk Function
MPS	Maximum Principal Strain
PMHS	Post-Mortem Human Subject
PS99	99th Percentile Element Strain
UN	United Nations
VRU	Vulnerable Road User
WHO	World Health Organization

Nomenclature

Below is the nomenclature of indices, sets, parameters, and variables that have been used throughout this thesis.
Below is the nomenclature of symbols and parameters used throughout this thesis.

Greek Symbols

ϵ	Strain
μ_i	Mean ultimate strain of age group i
σ_i	Standard deviation of ultimate strain of age group i
β	Weibull shape parameter
β_1	Age coefficient in Weibull AFT model
λ_0	Weibull scale parameter (characteristic failure strain)

Latin Symbols

n_i	Number of specimens in age group i
$P(\varepsilon \mid \text{Age})$	Probability of fracture at strain ε given age
x_{ij}	Synthetic failure strain of specimen j in age group i

Contents

List of Figures

List of Tables

1
Introduction

Road traffic accidents remains a major global health concern, causing more than a million fatalities and even more non fatal injuries each year worldwide. Even though a lot of improvements in road safety regulation was adopted road crashes remains the leading cause of death among children and young adults aged 5-29 years old, and it is also 12th leading cause of death globally as per a report published by WHO in 2023 [38]. It also reports that majority of these victims, around 56%, are vulnerable road users (VRUs) consisting of pedestrians, cyclists and motor cyclists.
To improve the safety on roads, in 2020, UN resolution named "Improving global road safety" was adopted with an ambitious aim to reduce the number of traffic deaths and injuries to half by the year 2030. This resolution represents a significant shift in ambition, given that as recently as the late 20th century it was widely believed that little could be done to protect pedestrians in the event of a vehicle impact [35].
To work towards the goal of reducing traffic deaths and injuries several safety systems like active bonnet, windshield airbags, to name a few, have been developed by car manufacturers to protect pedestrians [27]. In such automotive safety researches, several approaches are being used to study the biofidelic injury mechanisms of a human. These tests include, volunteer tests, post-mortem human subjects (PMHS) experiments, crash tests using anthropometric test devices (ATDs) [39], and more recently numerical simulations using detailed human body models (HBMs). With improvements in computational methods and available anatomical data, finite element method (FEM) based HBMs have become an essential tool in analyzing injury mechanics in complex impact scenarios.
State of the art HBMs like THUMS, GHBMC and SAFER HBM are widely used today in the automotive industry and in academic research to evaluate the vehicle safety systems. However, the predictive capabilities of HBMs are limited by the extent to which the model has been validated or by the availability of a proper injury criteria or injury risk functions. While the kinematic response of different body regions can be compared against biofidelic studies of human body ([8], [29]), the goal is to relate the obtained mechanical response from the simulation to the probability of sustaining a specific injury.

1.1 Motivation

In pedestrian-vehicle collisions, the lower extremities are among the most frequently injured body region [40]. As illustrated in figure 1.2, the first contact occurs between

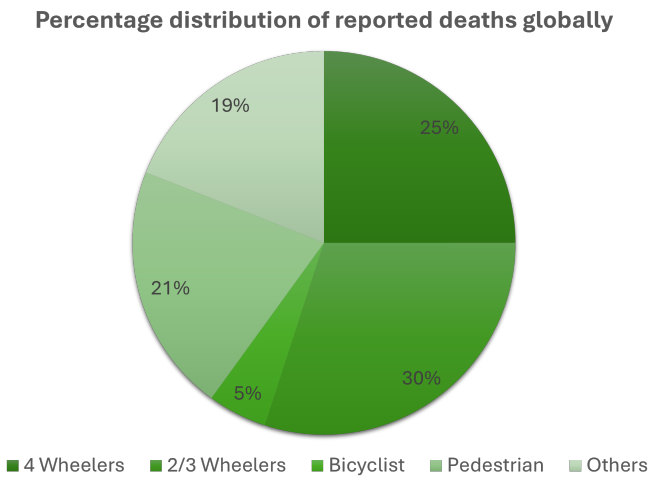

Figure 1.1: Percentage distribution of road traffic deaths by type of road user, globally (2021). Adapted from WHO Global Status Report on Road Safety 2023 [38]

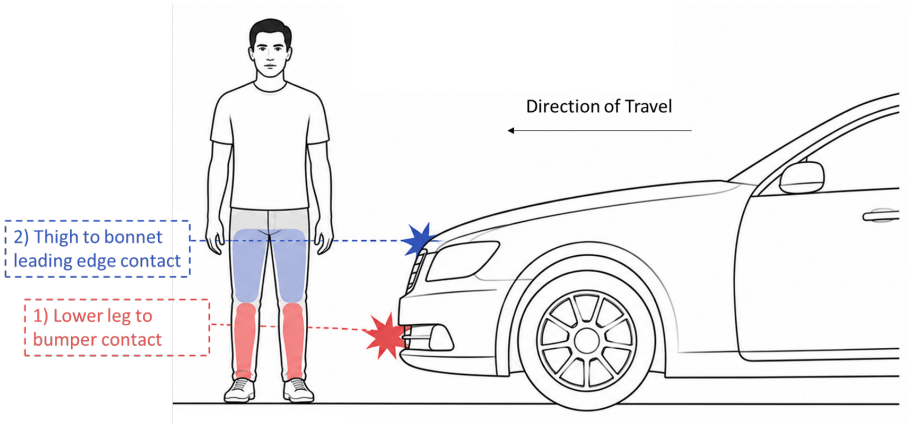

Figure 1.2: Contact sequence in a typical car-to-pedestrian collision showing (1) lower leg to bumper contact and (2) thigh to bonnet leading edge contact

the bumper and the lower leg followed by a secondary contact between thigh-to-bonnet leading edge. This loading sequence commonly results in fracture to long bones, particularly the femur and tibia. Even though such injuries are not life threatening they can lead to long term disability, inability or a lengthy delay in returing to pre injury activities. This leads to symptoms of depression and post-traumatic stress, and effectively reducing the quality of life [6].

In lower extremities, fractures to the long bone shaft represents a major injury outcomes in pedestrian-vehicle collisions [22]. While detailed FE models of the lower extremity exists, capable of translating the model's mechanical response into a quantitative fracture risk estimate remains absent for these bones in SAFER HBM. Such risk functions are derived from PMHS experimental data and relate relevant mechanical metrics to the probability of fracture.

Historically fracture assessment in impact biomechanics has relied on force or bending moment injury metrics obtained from whole experiments or ATD measurements.

However, these global quantities carry two fundamental limitations. First, they are strongly dependent on bone geometry. Identical applied forces will produce substantially different stress and strain states across specimens with different cross-sectional dimensions or cortical thickness. Second, they are sensitive to impact speed, as impact velocity increases, recorded forces and moments increase accordingly, even if the underlying tissue level deformation does not change proportionally. As a result, force and moment based IRFs derived under one set of experimental conditions may not generalize reliably to real world impact scenarios or across the population.

Strain based injury metrics address both of these limitations by directly quantifying tissue level deformation within the cortical bone. Maximum principal strain, extractable directly from cortical bone elements in FE simulations, captures the local mechanical state responsible for fracture initiation and is less dependent on specimen geometry or loading configuration. This makes it a more biofidelic and transferable injury predictor for use with HBMs.

Within SAFER HBM framework, previous development efforts have primarily been focused on injury prediction upper body regions where validated injury criteria and risk functions are mature [12]. To extend the capabilities to the pedestrian assessment there is a need to establish the injury risk functions for the femur and tibia.

1.2 Aim

This thesis focuses on the development and validation of the strain-based fracture injury risk functions for the femur and tibia, with the aim of enabling biofidelic fracture prediction in pedestrian vehicle impact simulations using the SAFER HBM. The work is guided by primary objectives:

- To develop strain based injury risk functions for the femoral and tibial shafts using probabilistic survival analysis applied to cortical bone coupon test data from the literature.
- To validate the developed injury risk functions through virtual reconstructions of isolated bone bending experiments and comparing the predicted risk to the fracture in the tests.

1.3 Ethical Considerations

The project relies on biomechanical reference data derived from post-mortem human subject testing reported in previous studies. No new experiments were conducted as part of this thesis. All data used for model validation are publicly available and were originally collected under established ethical guidelines at the time of the studies.

In the present work, previously published PMHS experimental data were used exclusively for the development and validation of injury risk functions aimed at improving fracture predictions for the lower extremities of the SAFER HBM. This work complies with Chalmers University of Technology's ethical policies and Volvo Car's internal guidelines on responsible research conduct.

1.4 Limitations

In this thesis, investigation is limited to lower extremity long bone shafts i.e. Femur and Tibia shafts, fracture risk under relevant loading condition for car-pedestrian impact. Injuries to soft tissue, ligaments, fibula and joints of the lower extremity are not considered. The injury risk function is developed using the previously published PMHS data. In this present work fracture is treated more as an injury outcome and variation in fracture pattern and fracture timing are not explicitly modeled. Additionally, the fracture behavior and injury mechanism for epiphysis region of both femur and tibia are not within the scope of this study.

2

Theory

This chapter explains some of the concepts used in this study to provide a basis of knowledge relevant in the rest of the study. From the Biological concepts used to the Statistical and mechanical concepts relevant to the study are mentioned here.

2.1 Human Lower Extremity Anatomy

The human lower extremity is a complex musculoskeletal structure primarily responsible for supporting body weight, maintaining balance and enabling locomotion [7]. It consists of pelvis, femur, patella, tibia, fibula and foot bones, connected through a network of joints, ligaments muscles and tendons. Among these structures, the femur and tibia are the main load bearing bones of the lower extremity and play a significant role in impact biomechanics.

2.1.1 Anatomical Terminology and Directions

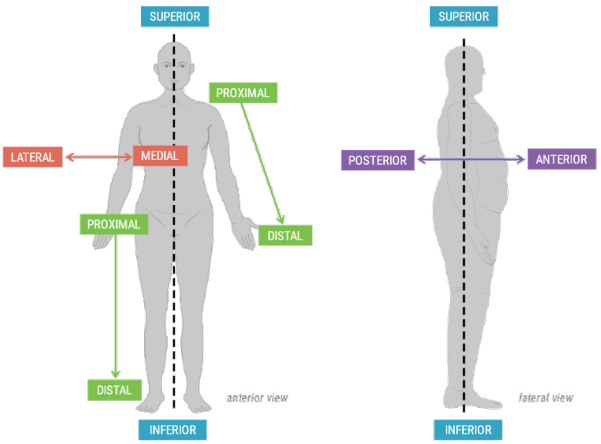

Figure 2.1: Directional Terms Applied to the Human Body. Paired, but opposite, directional terms are shown as applied to the human body at either end of the same arrow [23].

To describe the geometry, orientation and loading conditions of the human body consistently, standard anatomical terminology is used throughout this thesis. Anatomical directions are defined with respect to the anatomical position in which the body

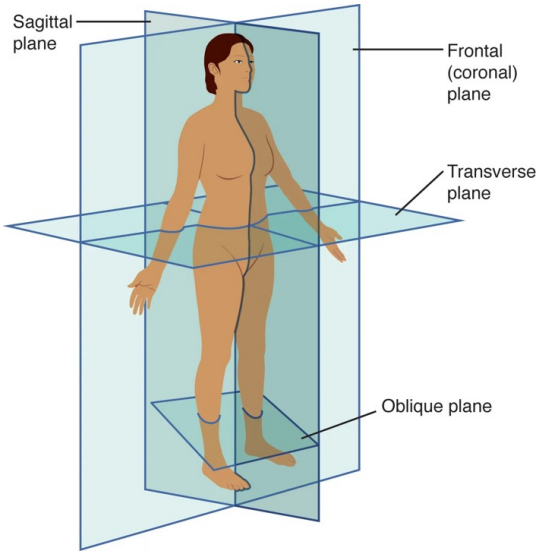

Figure 2.2: The three planes normally used to describe a human [1]

stands upright facing forward with arms at the side and palms facing forward as seen in figure 2.1.
The principal anatomical directions used in this work are anterior and posterior, referring to the front and back of the body respectively. Similarly, medial and lateral, refer to directions toward and away from the body midline, while proximal and distal refer to the directions closer to and farther from the trunk. Superior and inferior refer to directions toward the upper and lower parts of the body. Three principal anatomical planes are additionally used to define cross section and loading orientations as seen in figure 2.2. The sagittal plane divides body into left and right portions while the coronal plane into anterior and posterior portions and transverse plane into upper and lower portions. These reference conventions are essential for defining loading directions, boundary conditions, fracture orientation and stress distribution in a consistent and reproducible manner.

2.1.2 Anatomy of Femur

The femur is the longest and strongest bone in the human body and serves as the primary load-bearing structure of the thigh. It extends from the hip joint proximally to the knee joint distally and plays a crucial role in standing, walking and impact load transfer.
The proximal region of the femur consists of the femoral head, which articulates with the acetabulum of the pelvis to form the hip joint. The central portion of the femur, known as the diaphysis or shaft, is primarily composed of dense cortical bone that provides high stiffness and strength under bending and axial loading. The distal femur expands into the medial and lateral condyles, which articulates with the tibia at the knee joint.
Its structural behavior is strongly influenced by variations in cortical thickness and trabecular architecture.

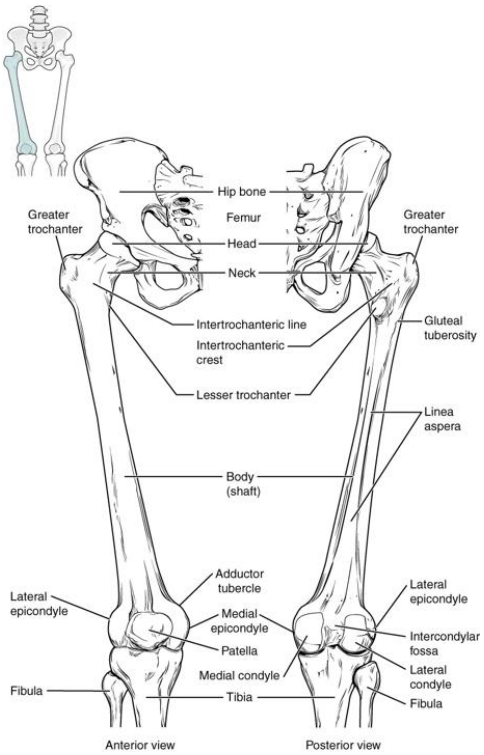

Figure 2.3: Anatomy of Femur [1]

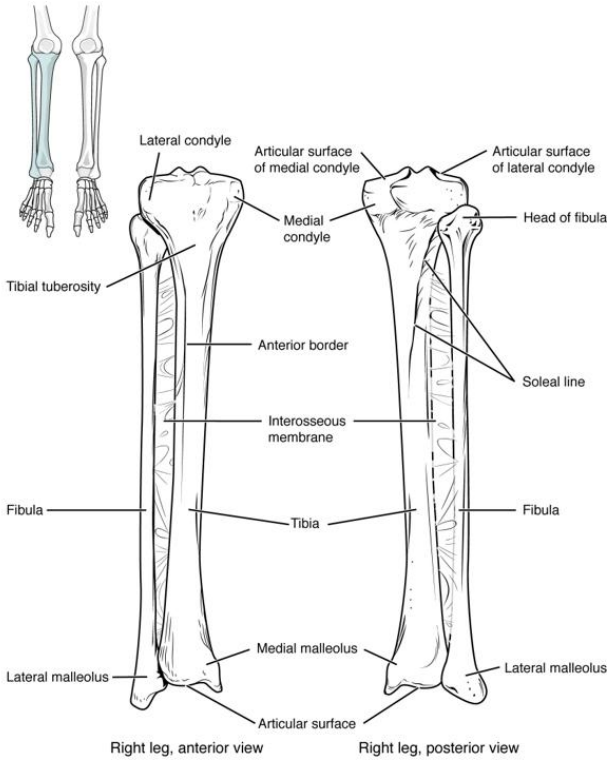

Figure 2.4: Anatomy of Tibia [1]

2.1.3 Anatomy of Tibia

The tibia is the primary weight bearing bone of the lower leg and is located medially to the fibula. It transfers loads from the femur to the ankle and plays a significant role in lower limb stability and locomotion.
The proximal tibia contains the medial and lateral tibial condyles, which articulates with the femoral condyles to form the knee joint. Below the proximal region is the tibial shaft, which has a triangular cross-sectional geometry and consists of cortical bone surrounding an inner trabecular and marrow region. The anterior border of the shaft is subcutaneous and commonly referred to as the shin. Distally, the tibia widens to form the medial malleolus at the ankle joint.
The structural composition of the tibia includes a dense cortical shell and an inner trabecular core as shown in figure 2.5, both of which contribute to its mechanical response.

2.2 Biomechanics of Long Bone Fracture

2.2.1 Long Bone Loading in Pedestrian Impact

Fractures of the long bone i.e, femur and tibia, represent severe lower extremity injuries frequently observed in pedestrian-vehicle impact. During primary impact phase, the bumper or leading edge of the bonnet contacts the lower extremity. This generates complex loading conditions involving bending, axial compression and

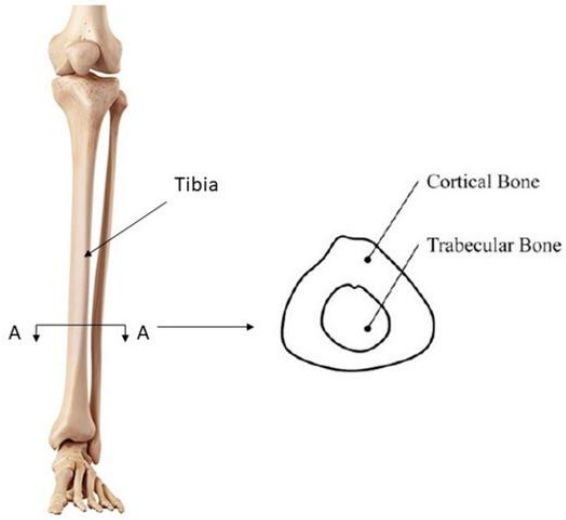

Figure 2.5: 3D view of the tibia bone and details of the bone cross-section highlighting the cortical and trabecular regions [5].

shear forces [36]. Due to the geometry and boundary conditions of the pedestrian's leg during impact, bending becomes dominant loading mechanism responsible for fracture initiation.

To reproduce this dominant fracture mechanism, simplified experimental loading configurations are commonly used under controlled conditions. Experimental investigations of femur and tibia generally utilize simplified bending configurations such as three-point and four-point bending setups to reproduce similar deformation modes in controlled environments. These configurations enable systematic investigation of fracture mechanisms, structural response, and strain distribution within the cortical shell. These configurations form the experimental basis for both injury data collection and FEM validation in the present work.

2.2.2 Fracture Mechanism

Long bone fracture is governed by both material level and structural level mechanisms. At the material level, fracture occurs when local tissue deformation exceeds the ultimate strain capacity of cortical bone. At the structural level, geometric factors such as cortical thickness, cross sectional area, and bone curvature influences stress distribution and crack initiation.

Under bending, the cortical shell experiences compressive loading on the impact side and tensile loading on the opposite side. Since cortical bone has lower tolerance in tension than in compression, fracture initiation typically occurs on the tensile surface [9], at the location of the highest principle strains. Once local microdamage accumulates beyond a critical level, crack propagation progresses through the cortical shell, ultimately leading to catastrophic structural failure.

2.2.3 Strain Based Injury Metrics

Traditionally, fracture assessment in impact biomechanics has relied on force or bending moment based measurements obtained from whole bone experiment. However, as discussed in section 1.1, these global quantities are strongly dependent on specimen geometry, boundary condition and loading condition, limiting their transferability across different loading conditions and population.
Strain based injury metrics provide a fracture risk by directly quantifying tissue-level deformation. Maximum principal strain within the cortical bone is therefore used as a fracture predictor in the present work. Unlike force based metrics, strain captures the local mechanical state responsible for tissue failures. In finite element human body models, strain based metrics can be extracted directly from the cortical bone elements during simulation. This enables injury assessment using tissue level quantities rather than purely external structural response.

2.3 Cortical Bone Mechanics

2.3.1 Material Behavior

Cortical bone is a hierarchical biological composite material primarily composed of mineralized collagen fibrils organized into osteonal microstructures. Due to this, cortical bone exhibits anisotropic mechanical behavior, meaning that its mechanical properties depend on the loading direction relative to the dominant osteon orientation.
The stress-strain response of the cortical bone typically consists of an initial linear elastic region which is followed by yielding, damage accumulation and eventual failure [26]. Important mechanical parameters governing this response are the elastic modulus, yield strain, and ultimate strain. The elastic modulus defines the stiffness of the tissue during elastic deformation, while the ultimate strain represents the deformation level at fracture initiation.
Cortical bone additionally exhibits viscoelastic and strain rate dependent behavior. Under dynamic loading conditions, stiffness increases relative to quasi-static loading. This behavior is particularly relevant for pedestrian impacts where loading duration occurs within milliseconds and deformation rates are substantially higher. At the macroscopic scale, cortical bone demonstrates greater compressive strength than tensile strength. Consequently, tensile failure typically governs fracture initiation during bending dominated loading. The heterogeneous structure of bone tissue also introduces considerable variability in measured mechanical properties between specimens.

2.3.2 Age Dependency

The mechanical behavior of cortical bone changes significantly with age. Age related modifications in mineral density, porosity, and collagen cross-link alter both stiffness and fracture tolerance [4, 28]. In particular, ultimate strain capacity decreases progressively with increasing age, resulting in more brittle fracture behavior in elderly

population.
Experimental studies have reported reductions in ultimate strain by approximately 10-12% per decade [4]. These reductions are accompanied by increased cortical porosity and decreased energy absorption capability. Since pedestrian injury risk strongly depends on the age distribution of the population, ignoring age effects may lead to systematic under prediction of fracture risk in older individuals and over prediction in younger populations. Therefore, age adjusted probabilistic IRF are essential for population representative injury assessment.

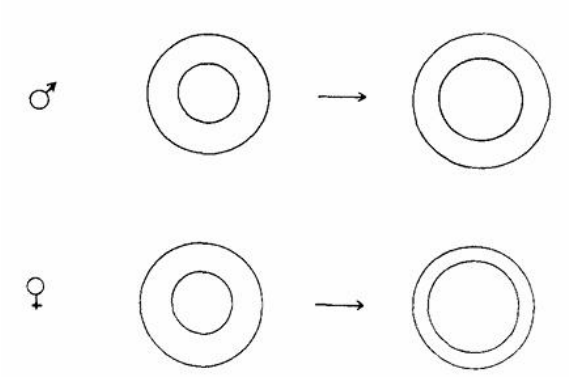

Figure 2.6: Schematic representation of cortical bone remodeling with age in males and females [33].

2.4 Experimental Characterization

2.4.1 Coupon Testing

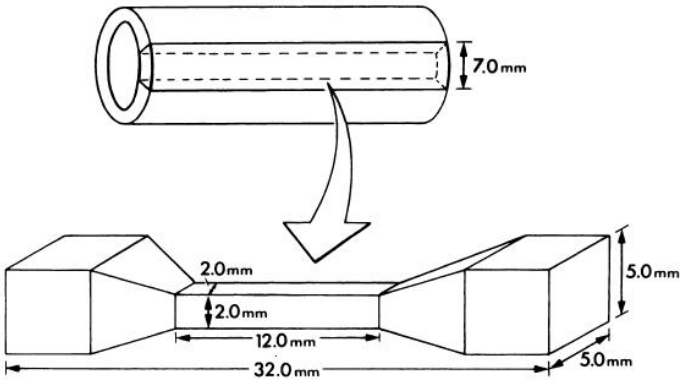

Figure 2.7: Schematic diagram showing the dimensions of the cortical specimens and of one of the areas of the femoral diaphysis from which the specimens were taken [26].

Coupon tests are commonly used to characterize the mechanical properties of cortical bone at tissue level while minimizing structural and geometric influences. In these experiments, small cortical bone specimens are extracted from the diaphyses of long bones and subjected to controlled uniaxial loading conditions until failure [18, 19].

Specimens are typically machined into standardized geometries to ensure uniform stress distribution. Strain is measured directly using strain gauges positioned over gauge length, enabling accurate determination of elastic modulus, yield strain and ultimate strain.
Compared to whole bone experiments, coupon tests isolate intrinsic material behavior and provide individual level measurements suitable for statistical analysis. These data are particularly valuable for probabilistic injury modeling because it enables direct characterization of variability is tissue failure properties.
However, many historical coupon test studies report results only in aggregated form, providing summarized statistics such as mean and standard deviation of mechanical properties along with the sample size of the study [3]. This limitations complicates direct probabilistic modeling and motivates use of statistical reconstruction techniques to generate synthetic individual level dataset consistent with reported experimental statistics.

2.4.2 Whole Bone Bending Test

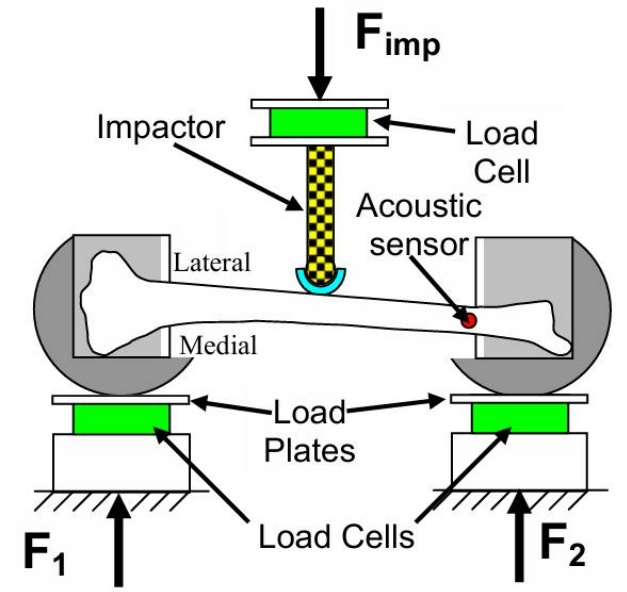

Figure 2.8: Schematic representation of whole bone bending test [20].

Whole bone experiments investigate the structural response of intact long bones under loading conditions relevant to injury biomechanics. In injury biomechanics, three point and four point bending tests are commonly used to reproduce the fracture mechanisms observed in pedestrian impacts [14, 11].
In these experiments, force and displacement are recorded throughout the loading until fracture occurs. Unlike coupon tests, whole bone experiments capture the combined influence of geometry, cortical thickness distribution and material properties on structural response.
Many studies provide specimen level force-time or force-displacement histories together with fracture outcomes, making them valuable for FEM validation. By re-

producing the experimental loading conditions numerically, local cortical strain distribution can be extracted from simulations and compared against experimentally observed fracture behavior.

Consequently, whole bone experiments serve as an important structural validation framework for evaluating the predictive capability of strain based injury metrics and probabilistic fracture risk functions under realistic loading conditions.

2.5 Statistical Reconstruction of Aggregated Data

In biomechanical research, experimental datasets are often reported in aggregated form, providing only mean, standard deviation and sample size for the group of specimen divided by age groups. While such summaries are informative, they do not provide the individual level observations required for probabilistic survival modeling, where each data point must carry both failure value and a covariate such as age.

Statistical reconstruction addresses this by generating synthetic individual level datasets that are statistically consistent with the reported group level summary. For a given age group i with the reported mean μ_i, standard deviation σ_i and sample size n_i, synthetic observations are drawn from a normal distribution.

$$x_{ij} \sim \mathcal{N}(\mu_i, \sigma_i^2), \quad j = 1, \ldots, n_i \tag{2.1}$$

where each synthetic realization x_{ij} represents the failure strain of a hypothetical specimen. To represent age dependency continuously rather than in discrete groups, the reported summary statistics are linearly interpolated across age prior to sampling. allowing the reconstruction to reflect a smooth age-strain relationship.

Because each synthetic dataset represents only one plausible realization of the underlying population, a single reconstruction is in sufficient to characterize the uncertainty introduced by working from aggregated data. A Monte Carlo framework is therefore employed, in which the reconstruction and subsequent model fitting are repeated a large number of times (n=500) each producing a different synthetic dataset drawn from the same reported statistics. For each realization, a separate parametric Weibull survival model is fitted using maximum likelihood estimation, incorporating age as a covariate. Each fitted model also produces its own parametric Confidence Interval (CI), computed within the flexsurv [15] package of R software.

The final injury risk function is then obtained by averaging the predicted risk values across all 500 Monte Carlo realizations at each strain and age value of interest. The uncertainty bounds of the final curve reflect the combined variability arising from both the parametric confidence intervals of individual model fits and between realization spread introduced by reconstruction itself. This approach yields a robust probabilistic injury risk function that accounts for the inherent uncertainty associated with reconstructing individual level data from aggregated experimental sources.

2.6 Injury Risk Functions using Survival Analysis

Injury risk functions express the probability of fracture as a function of a mechanical metric using statistical models. In survival analysis, the failure variable is the strain at which fracture is predicted to occur, and the injury risk function gives the cumulative probability of fracture at a given strain level.
The Weibull distribution is commonly applied in biomechanical injury modeling due to its flexibility in capturing a wide range of failure distributions and its straightforward incorporation of covariates. The age-dependent Weibull injury risk function takes the form:

$$P(\epsilon|\text{Age}) = 1 - \exp\left[-\left(\frac{\epsilon}{\lambda_0 e^{\beta_1 \cdot \text{Age}}}\right)^{\beta}\right] \tag{2.2}$$

where ϵ is the maximum principal strain, λ_0 is the scale parameter representing the characteristic failure strain of a reference population, β is the shape parameter controlling the steepness of the risk curve and β_1 is the age coefficient capturing the shift in the fracture tolerance with increasing age. Model parameters are estimated by maximum likelihood.
In a Weibull accelerated failure time (AFT) model, the logarithm of the characteristic fracture tolerance is expressed as a linear function of the covariates. The age coefficient, β_1, therefore represents the effect of age on the logarithm of the characteristic fracture tolerance. Exponentiation of the coefficient yields a time ratio, which describes the multiplicative change in fracture tolerance associated with a one-unit increase in age [16].
To facilitate interpretation, the effect of age was expressed as the percentage change in characteristic fracture tolerance associated with a 10-year increase in age:

$$\text{Age Effect } (\%) = 100\,[\exp(10\beta_1) - 1] \tag{2.3}$$

where β_1 is the estimated age coefficient from the Weibull AFT model. Negative values indicate a reduction in fracture tolerance with increasing age, while positive values indicate an increase. For example, an age coefficient of $\beta_1 = -0.00988$ corresponds to a decrease in characteristic fracture tolerance of approximately 9.4% per decade.

2.7 Finite Element Validation Framework

Validation is critical requirement for establishing confidence in any FE based injury prediction methodology. In the context of strain based fracture risk assessment, validation serves two distinct purposes. One is that it confirms that the FE model reproduces the experimentally observed structural response with sufficient fidelity, and secondly, confirming that the strain values extracted from the validated model produce fracture risk predictions consistent with the observed experimental outcomes.
A component level validation strategy is adopted in the present work, in which isolated bone models are simulated under experimentally controlled bending con-

figurations rather than within a full body impact simulation. This approach offers several advantages. It allows direct comparison between simulated and experimentally measured force-time histories, which serve as the primary indicator of structural biofidelity. It reduces modeling complexity by removing the influence of surrounding soft tissues, joint interactions and full body kinematics allowing the evaluation to focus specifically on the mechanical behavior of the cortical bone.
Validation is considered successful when the simulated force time response falls within the corridor of experimental measurements, and when the cortical strain extracted at the time of experimentally observed fracture produces a fracture probability above 50% when evaluated against the developed injury risk function. The validated component level framework then forms the bases for integration into full body pedestrian simulation.

2.8 SAFER Human Body Model

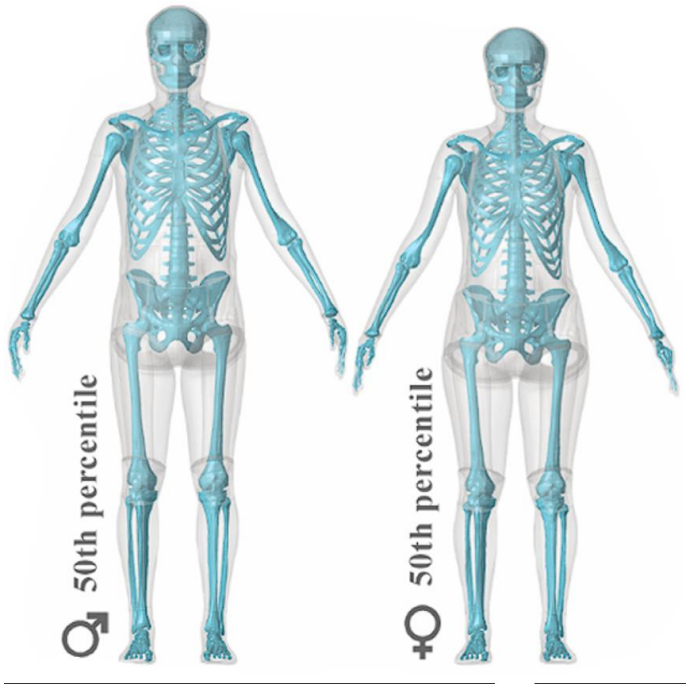

Figure 2.9: Baseline male and female SAFER pedestrian HBM [25]

The SAFER HBM was founded by Chalmers University of Technology, Autoliv and Volvo Cars. It is further developed and brought to market by the Fraunhofer Chalmers Centre, together with the founding organizations, to promote safety and innovation for the greater good. This serves as the target platform for the IRF developed in this thesis.
The model incorporates anatomically detailed representations of the skeletal structures, major soft tissue regions, and internal organs. The lower extremity is represented with separate cortical and trabecular bone regions for the femur and tibia, with the cortical shell modeled using solid elements that allow extraction of local

strain fields during simulation. This architecture is directly compatible with the strain based injury assessment framework developed in the present work, as maximum principal strain can be extracted element wise from the cortical bone regions during any impact simulation.

3
Methods

The methods used for the study are described in this chapter along with related data and images to provide examples. The Injury Risk Curve generation methodology along with details about the FE Setup are presented here.

3.1 Injury Risk Curve Generation

3.1.1 Data Sources and Preparation

The injury risk function was developed using cortical bone coupon test data obtained from Burstein et al. [3] and McCalden et al. [26]. These datasets were selected based on their relevance to femur and tibia fracture mechanics and availability of strain-at-failure measurements together with specimen age information.

The datasets were used in a bone-specific manner. For tibia, only the Burstein dataset was available and therefore used exclusively. For the femur, both datasets were available and were combined to increase the total sample size and improve representation of inter-specimen variability across the population.

McCalden dataset provides individual specimen level measurements, including the age and corresponding failure strain for each of the 46 PMHS specimen tested, and was therefore used directly in the analysis without reconstruction. The Burstein dataset, in contrast, reports results in aggregated form, providing mean and standard deviation of ultimate strain for groups of specimen divided decade of age, covering ages from range of 20s through the 80s, along with the total number of PMHS specimen, which was 33 for femur and 28 for tibia. To enable probabilistic modeling from this aggregated source, the Burstein data were reconstructed into synthetic individual level dataset using the statistical method describe in Section 2.5

For the Burstein dataset, the reported number of PMHS specimens was used when generating synthetic datasets. Multiple coupon tests from the same PMHS were not treated as independent samples, ensuring that each reconstructed observation corresponds to a unique specimen and avoiding artificial inflation of the effective sample size.

Prior to model development, all datasets were harmonized into a consistent format, and entries with missing strain or age information were excluded. The datasets used contained measures of engineering stress, σ_{eng} and engineering strain, ε_{eng}. FE Simulations output true stress, σ_{true} and true strain, ε_{true} and thus, the values were recomputed according to equation 3.1 and 3.2.

$$\sigma_{true} = \sigma_{eng}(1 + \varepsilon_{eng}) \tag{3.1}$$

$$\varepsilon_{true} = \log(1 + \sigma_{eng}) \tag{3.2}$$

Table 3.1: Overview of the available coupon test data.

Paper	Bone targeted	Number of PMHS
Burstein et al. [3]	Femur Cortical Bone	33
Burstein et al. [3]	Tibia Cortical Bone	28
McCalden et al. [26]	Femur Cortical bone	46

3.1.2 Reconstruction of Aggregated Data

The aggregated data reported by Burstein et al. were transformed into individual-level datasets using the statistical reconstruction methodology described in Section 2.5. To represent age dependency continuously rather than in discrete decade level groups, the reported summary statistics were linearly interpolated across age prior to sampling. This interpolation allows each synthetic specimen to be assigned a smoothly varying failure strain consistent with its age, rather than being assigned the group mean of a broad age bracket.
A Monte Carlo approach was adopted to account for uncertainty associated with this reconstructing individual level data from aggregated sources. A total of 500 synthetic datasets were generated, each representing a plausible realization consistent with the reported experimental statistics.
For the femur, each Monte Carlo realization combine the reconstructed Burstein samples and McCalden specimen-level data. Specifically, each realization included 33 PMHS samples derived from Burstein and 46 samples from McCalden, resulting in a total of 79 samples per dataset. For the tibia, each realization consisted solely of 28 synthetic PMHS observation reconstructed from the Burstein dataset.

3.1.3 Model Fitting Procedure

A parametric Weibull survival model, as described in Section 2.6, was fitted to each of the 500 Monte Carlo datasets for both femur and tibia. In this framework, ultimate strain is treated as the failure variable, and age is included as a continuous covariate to account for its influence on fracture tolerance. All specimens were assumed to have experienced failure, meaning no censoring was applied. Model fitting was performed using the maximum likelihood estimation, implemented through the `flexsurv` package in the R software [15]. Each fitted model additionally produced parametric confidence intervals reflecting statistical uncertainty of individual realization.
The confidence bands reported for each injury risk curve were derived using a parametric method. For each fitted Weibull model, pointwise confidence intervals were

computed directly from the maximum likelihood estimates of the model parameters and their associated variance-covariance matrix, as implemented through the `flexsurv` package in R [15]. At each strain value, the confidence interval on the predicted survival function was obtained by applying the delta method to propagate parameter uncertainty through the nonlinear Weibull expression, yielding upper and lower bounds on the fracture probability. In the Monte Carlo framework, each of the 500 realizations produced its own set of parametric confidence intervals. The final confidence band displayed on the mean injury risk curve was obtained by averaging the upper and lower bounds of the parametric confidence intervals across all 500 realizations, capturing both the within-realization parametric uncertainty and the between-realization variability introduced by the statistical reconstruction of aggregated data.

3.1.4 Monte Carlo Curve Generation and Final Representation

For each of the 500 fitted Weibull models, injury risk curves were evaluated over a predefined strain range at representative age values of 25, 45 and 65 years. These ages were selected because they represent an even spread across the adult population and are consistent with age values used in previous injury assessment work within the SAFER HBM framework [2].
The final injury risk function for each bone was obtained by averaging the predicted fracture probability values across all 500 Monte Carlo realization at each strain and age points. The uncertainty bounds of the final curves were derived from the combined spread of individual realization confidence intervals and the realization variability introduced by the reconstruction process, providing a comprehensive representation of the uncertainty associated with working from aggregated experimental data.

3.2 Finite Element Simulation Setup

3.2.1 Modeling Approach

A component level validation strategy was adopted, in which isolated femur and tibia models were simulated under experimentally controlled bending configurations. As described in Section 2.7, this approach allows direct comparison between simulated and experimentally measured force time histories, and enables extraction of local cortical strain distributions for injury risk evaluation, without the complexity associated with full body impact simulation.
All finite element simulations were performed using LS-DYNA, an explicit finite element solver widely used in automotive crash and injury biomechanics applications. The choice of a strain based injury metric over force or moment based criteria was motivated by the limitations of global responses in Sections 1.1 and 2.2.3. Local maximum principal strain, extracted directly from cortical bone elements, was selected as primary output quantity for injury assessment, as it reflects the tissue

level deformation state responsible for fracture initiation independently of specimen geometry or loading configuration.
The validated component level framework developed here is intended to serve as a basis for integrating the strain based fracture risk functions into full body pedestrian simulations using the SAFER HBM.

3.2.2 Experimental Studies

The experimental studies used for the finite element validation were selected based on their relevance to bending dominated long bone fracture in pedestrian impact scenarios, and on the availability of sufficiently detailed experimental information to enable reliable numerical replication. A minimum requirement for inclusion was the availability of specimen geometrical details, loading configuration, boundary conditions, impact velocity or displacement input and measured force-time response. Studies lacking this level of details were excluded, and insufficient experimental information prevents the establishment of reliable boundary conditions in the finite element model.
Based on these criteria, the four point bending experiments of isolated human tibiae reported by Harden et al. [11] and the three point bending experiment of isolated femur reported by Ivarsson et al. [14] were selected for component level validation. A summary of both experimental setups is provided in Table 3.2

Table 3.2: Overview of the Selected Experiments.

	Ivarsson et al. [14]	Harden et al. [11]
Bone	Femur	Tibia
Loading Configuration	Three point bending	Four-point bending
Loading Plane	Sagittal	Lateral-Medial
Impactor Speed	1.5 m/s	6 m/s

3.2.2.1 Isolated Femur - Ivarsson et al. (2009) [14]

The femur loading configuration was based on the experimental work by Ivarsson et al. [14], in which isolated femoral shafts from PMHS were subjected to axial compression, sagittal plane bending and combined loading conditions. As the present work focuses solely on pedestrian safety, only the sagittal plane bending loading condition is considered here. The proximal and distal ends of the femur were rigidly potted and mounted on servo-hydraulic material testing machine, with loading introduced through a rigid impactor contacting the shaft in the sagittal plane. Instrumentation included strain gauges on the cortical surface and load cell integrated within the test setup. A foam pad was placed between the impactor and the bone surface to distribute the contact force. The study provided detailed descriptions of specimen preparation, loading conditions and fracture response, enabling reliable replication within the finite element framework.

3.2.2.2 Isolated Tibia - Harden et al. (2021) [11]

The tibia loading configuration was based on the experimental study conducted by Harden et al. [11]. Isolated human tibiae were dynamically loaded in a lateral-medial four point bending configuration reproducing loading conditions representative of the pedestrian lower extremity impacts. The proximal and distal ends of each tibia were rigidly potted at approximately 20% and 80% of the total bone length respectively, and the dynamic loading was introduced through two impact locations positioned at approximately 40% and 60% of the shaft length, generating a bending dominated loading state in the mid diaphysis region. The impact velocity was set to 6 m/s. No foam was used between the impactor and the bone surface, meaning the impactor contacted the cortical surface directly. Force response during the impact was recorded using the load cells positioned beneath the supports, while strain gauges attached to the cortical surface were used to monitor fracture timing.

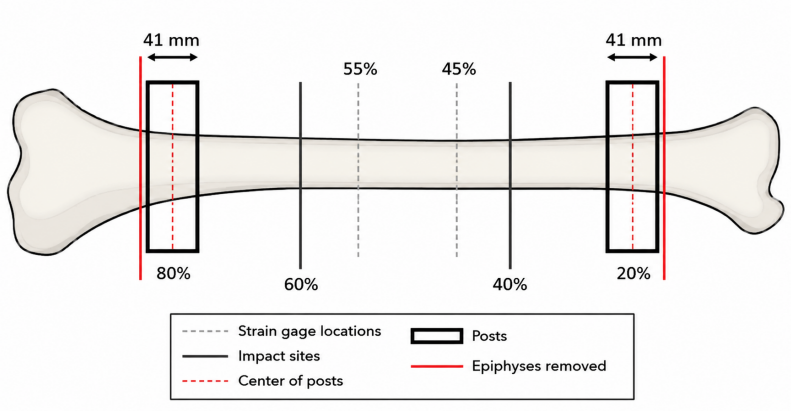

Figure 3.1: Schematic of bone specimen test setup showing pot locations, impact sites, and strain gage placement

3.2.3 Finite Element Model Preparation

3.2.3.1 Geometry Extraction and Processing

The femur and tibia FE models were extracted from the SAFER HBM and isolated for component level simulation. The cortical and trabecular bone regions defined within the original model were retained during preprocessing to preserve anatomical representation and structural characteristics of the long bone.
Since the experimental specimens used by Harden et al. and Ivarsson et al, had specific geometric dimensions that differed from those of the SAFER HBM 50th percentile male, a morphing procedure was applied to each bone model. The morphing targeted four geometric parameters measure from the experimental specimen description, total bone length, lateral-medial diameter, posterior-anterior diameter and cortical cross sectional area. These parameters were selected as they are the primary geometric determinants of bending stiffness and cortical strain distribution under applied loading conditions. CT scan data and fracture location information were not available for the experimental specimens, meaning that exact cortical thickness distribution and cross sectional shape could not be reproduced. Therefore, the

morphed geometry represents the best achievable approximation given the available experimental information, and this simplification is acknowledged as a source of uncertainty in local strain predictions.
Following morphing, the isolated bone geometries were positioned according to the respective experimental loading configurations described in the reference studies.

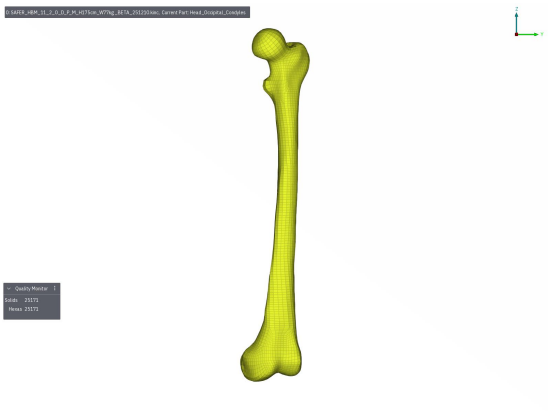

Figure 3.2: SAFER Femur Model

Figure 3.3: SAFER Tibia Model

3.2.3.2 Finite Element Mesh

The finite element mesh consisted of 8-node fully integrated hexahederal solid element representing the cortical and trabecular bone regions. The femur model contained approximately 25000, elements while the tibia model contained approxiamtely 14000 elements.
To enable accurate extraction of maximum principal strain at the outer cortical surface a thin membrane of 0.1 mm was applied to the outer surface of the cortical bone region in both femur and tibia models. The membrane was assigned the same material properties as the underlying cortical bone solid elements to ensure it did not alter the structural response of the model. Maximum principal strain values used for injury risk evaluation were extracted from this membrane layer through out the simulation duration.
Following the morphing procedure, mesh quality was evaluated across the bone using standard quality metrics including aspect ratio, warpage, skewness and Jacobian [32]. No elements with negative volumes or abnormal distortion relative to surrounding elements were identified.
The cortical bone material behavior was represented using the elastic-plastic material model `MAT_PIECEWISE_LINEAR_PLASTICITY` (`MAT024`) in LS-DYNA. This model was selected for its numerical robustness, computational efficiency, and ability to reproduce both the elastic and post yield behavior of cortical bone without requiring complex damage or fracture propagation formulations.
Material parameters were derived from the tensile material properties reported by Burstein et al. [3] for the 40-49 year age group, as this decade corresponds most closely to the age of 50th percentile male represented by the SAFER HBM. The elastic modulus, yield stress and plastic hardening behavior were defined based on

these reported values. Simplified isotropic material behavior was assumed throughout, consistent with the bending dominated loading conditions of the present study. Under bending, the primary stress and strain components act along the longitudinal axis of the bone, which corresponds to the dominant osteon orientation in cortical bone. The isotropic assumption therefore introduces minimal error under these specific loading conditions, while substantially reducing modeling complexity compared to a full anisotropic formulation. Since the goal of the present work was the extraction of fracture-relevant strain measures rather than explicit fracture propagation modeling, no element erosion or material failure criterion was implemented.

3.2.4 Simulation Setup

3.2.4.1 Femur 3-point Bending Simulation

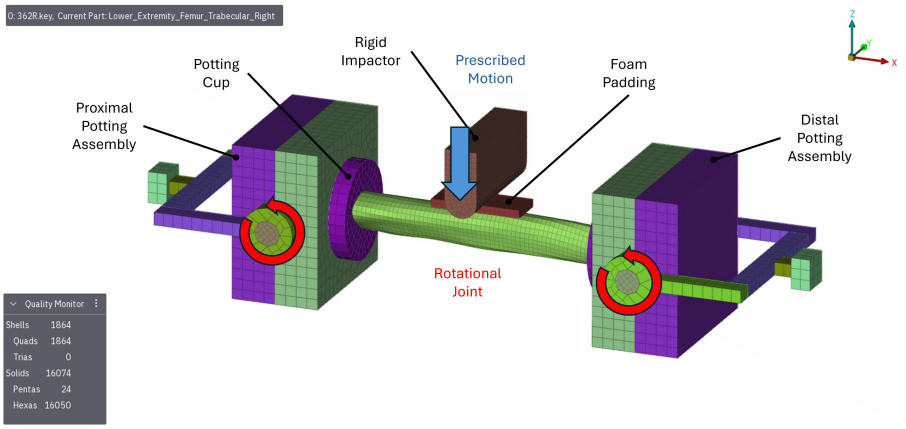

Figure 3.4: Simulation setup for femur three-point bending.

The femur simulation was developed based on the experimental configuration reported by Ivarsson et al [14]. The meshed loading assembly, including the loading fixture, rigid supports, foam properties and contact definitions, was adopted from the simulation setup published by Schubert et al [34]. and made available through the OpenVT platform, with modifications applied to accommodate the morphed femur geometry.

The femur model was positioned within the fixture according to the experimentally reported sagittal plane bending configuration. Dynamic loading was applied through a rigid impactor contacting the shaft region, with a prescribed displacement boundary condition applied to the impactor consistent with the experimental input. A foam material was included between the impactor face and the cortical bone surface, replicating the energy-absorbing layer used in the physical experiment. Contact interactions between the impactor, foam, and cortical bone surface were defined using automatic surface-to-surface contact formulations available in LS-DYNA.

3.2.4.2 Tibia 4-point Bending Simulation

The tibia finite element simulation was developed based on the experimental configuration reported by Harden et al. [11]. The meshed loading assembly, including impactors, support structures and contact definitions, was adopted from the numerical models presented by Weißenbacher [37] in their Master Thesis, with necessary modifications to accommodate the morphed tibia geometry used in the present work. The isolated tibia model was positioned within loading fixture according to the experimental configuration. Dynamic loading was introduced through rigid cylindrical impactors positioned at the prescribed loading locations, with a velocity boundary condition of 6 m/s prescribed to the impactors to replicate the experimental impact conditions. The impactors contacted the cortical bone surface directly, consistent with the experimental setup of Harden et al. in which no foam or soft tissue surrogate was used. Surface-to-surface contact definitions were implemented between the impactors and cortical bone surface.

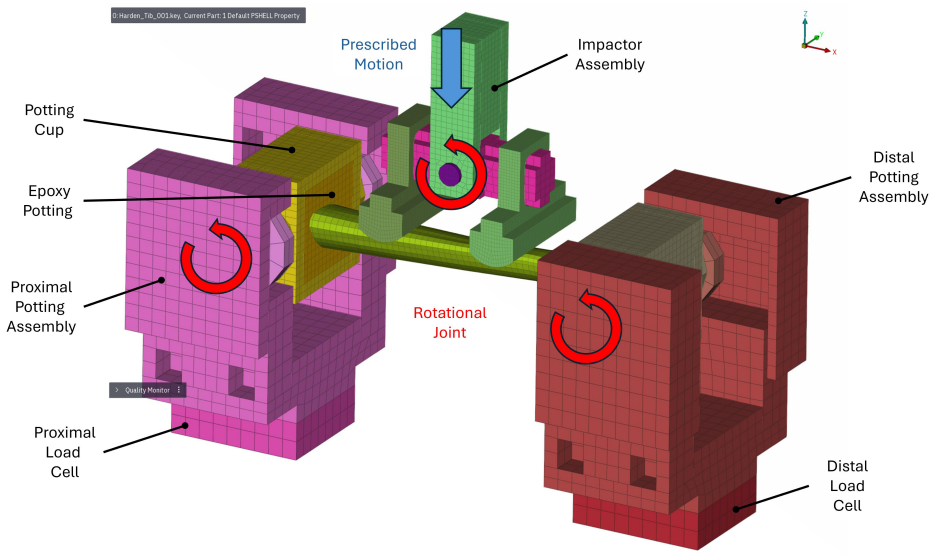

Figure 3.5: Simulation setup for tibia four-point bending

3.2.5 Output Parameters

Impactor force was extracted for the femur setup and forces for the tibia setup were taken as a summation of the load cell forces in z direction. Force-time histories were extracted from the rigid impactors and support structures throughout the simulation duration and used for comparison against the experimental measurements reported by Harden et al. and Ivarsson et al. Agreement between simulated and experimental force-time response was used as the primary indicator of model biofidelity.
For injury assessment, cortical bone strain distributions were extracted throughout the loading duration. Maximum principal strain was selected as the primary injury metric, consistent with its role as the fracture predictor in the developed injury risk functions and its established relationship with tensile fracture initiation in cortical bone under bending-dominated loading.

Maximum principal strain was extracted at the peak element value across the cortical bone region at each time step and used as the primary input to the injury risk evaluation. Additionally, the 99th percentile element strain was extracted to assess whether the peak strain values were influenced by localized numerical effects such as element distortion or contact instabilities. Close agreement between the peak and 99th percentile values would confirm that the strain field in the critical cortical region was physically meaningful and not dominated by isolated numerical artifacts.

4

Results

This chapter presents the results from the study and reports the findings. The injury risk curve parameters and graphs along with FE model comparison and results are mentioned here. This is followed by a final strain injury risk calculation.

4.1 Injury Risk Curve Results

4.1.1 Femur Weibull Injury Risk Curves

The Weibull survival analysis model described in Section 3.1 was applied to develop strain based femur fracture injury risk functions using the McCalden dataset, the reconstructed Burstein dataset and a combined dataset incorporating both sources. For each dataset, age was included as a continuous covariate in the Weibull model, and 500 Monte Carlo realizations were generated for all analyses involving the reconstructed Burstein data.

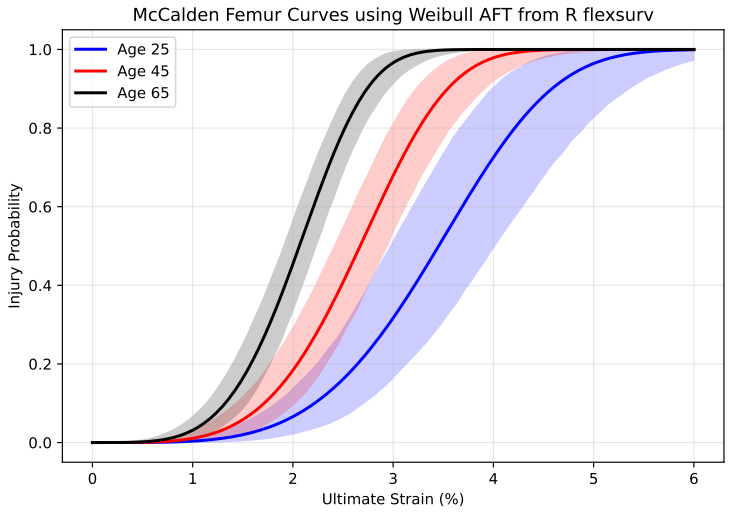

Figure 4.1: Femur fracture injury risk curves developed using the McCalden et al. dataset for representative age groups.

The derived injury risk curves from the McCalden dataset are shown in figure 4.1. The curves increase monotonically with strain across all age group and it showcases a clear age dependency, with curves corresponding to higher ages shifted toward lower strain values indicating a greater fracture risk in older populations. The 50% fracture probability is reached at approximately 3.5%, 2.5% and 2.1% ultimate

strain for the 25, 45 and 65 year age groups respectively. The confidence bands are widest for the youngest age group and progressively narrows with increasing age. This pattern indicates the relative smaller number of young specimen in McCalden dataset.

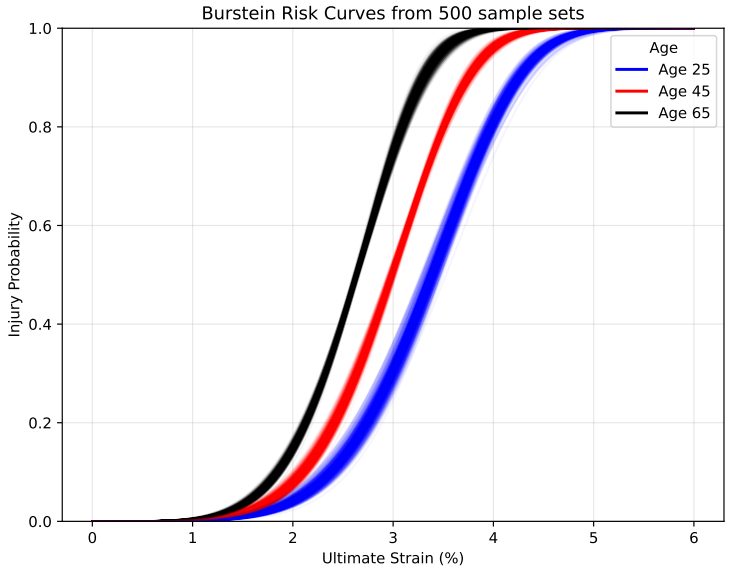

Figure 4.2: Femur fracture injury risk curves developed using the reconstructed Burstein et al. dataset.

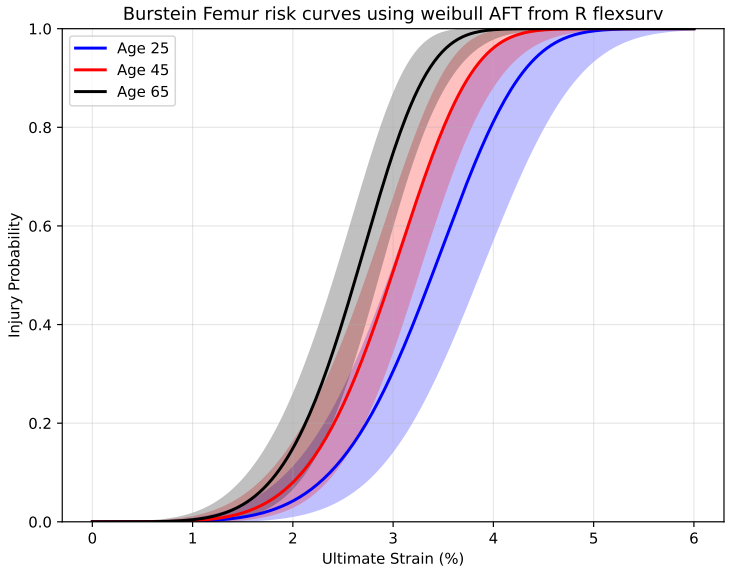

Figure 4.3: Femur fracture injury risk curves derived from the reconstructed Burstein dataset, showing mean curves and confidence bands.

The injury risk curve derived from the 500 Monte Carlo realizations reconstructed Burstein dataset are shown in figure 4.2. The individual realization curves are tightly clustered at each age group, indicating the reconstruction process produced Weibull

fits with small variability across realization. The age separation between the three groups is visibly smaller than in the McCalden curves, indicating a weaker age effect captured by the Burstein dataset alone.

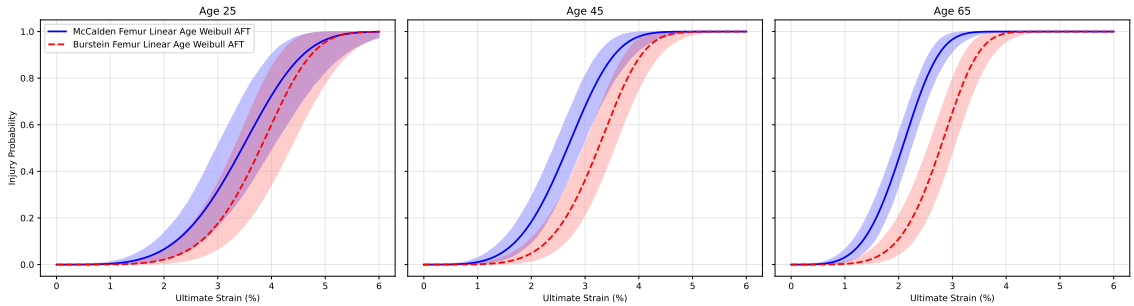

Figure 4.4: Comparison of femur injury risk curves derived from McCalden and Burstein datasets.

The mean curves and corresponding confidence band obtained by averaging across all 500 realizations of the Burstein dataset are shown in figure 4.3. The mean curves exhibit smooth monotonic behavior across the strain range. The confidence bands are broader at higher strain values, which is consistent with increased uncertainty in the tail of the distribution where fewer specimen contribute data.

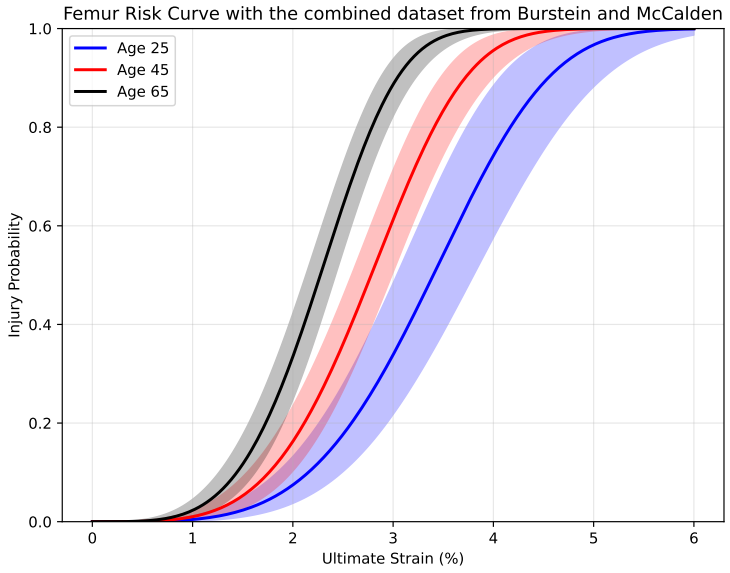

Figure 4.5: Final femur fracture injury risk curves developed using the combined McCalden and Burstein datasets.

A direct comparison between the McCalden and Burstein derived curves at each representative age is presented in figure 4.4. The two datasets show reasonable agreement for the 25 year age group, although the slope of the curve differs, with Burstein curve being steeper. For the 45 and 65 year groups, the slopes are more similar between datasets, but the McCalden curves consistently show a more pro-

nounced age effect, with greater leftward shift between age groups compared to the Burstein curves.

The final femur injury risk curves derived from the combined McCalden and Burstein dataset are shown in figure 4.5. The 50% probability is reached at approximately 3.5%, 2.9% and 2.25% ultimate strain for the 25, 45, and 65 year age group respectively. The confidence bands are narrower compared to either individual dataset, indicating the effect of increased effective sample size achieved by combining two sources within the Monte Carlo framework.

4.1.2 The Tibia Injury risk curves

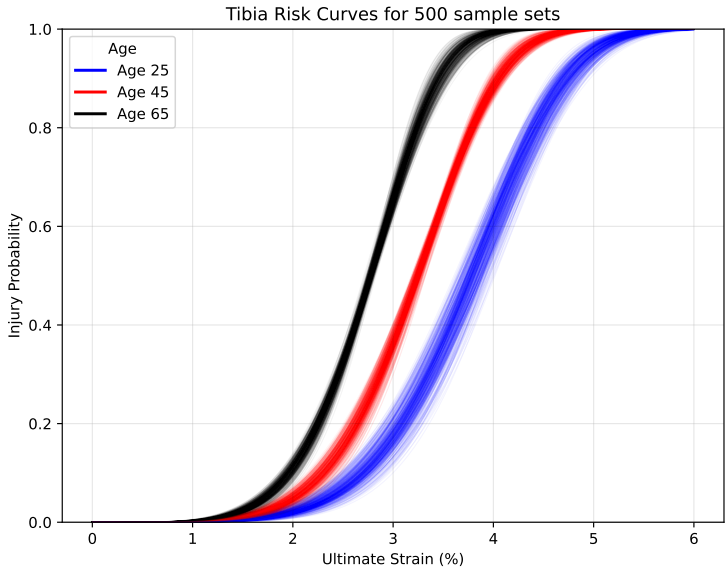

Figure 4.6: Tibia Risk Curves from the 500 sample sets generated from the Burstein parameters.

The tibia fracture injury risk function was developed using the reconstructed Burstein dataset, following the same Monte Carlo framework applied to the femur. The injury risk curves from all 500 Monte Carlo realization are shown in figure 4.6. The individual realization curves are tightly clustered at each group, indicating that the realization produced Weibull fits with small variability across realization.

The curves demonstrate a clear increase in fracture probability with increasing cortical strain as well as increasing age. The 50% fracture probability is reached at approximately 3%,2.5% and 2% strain for the 25, 45 and 65 year age groups respectively. The age separation and overall curve shape are broadly comparable to those observed in the Burstein femur curves, which is expected given the shared data sources and reconstruction methodology.

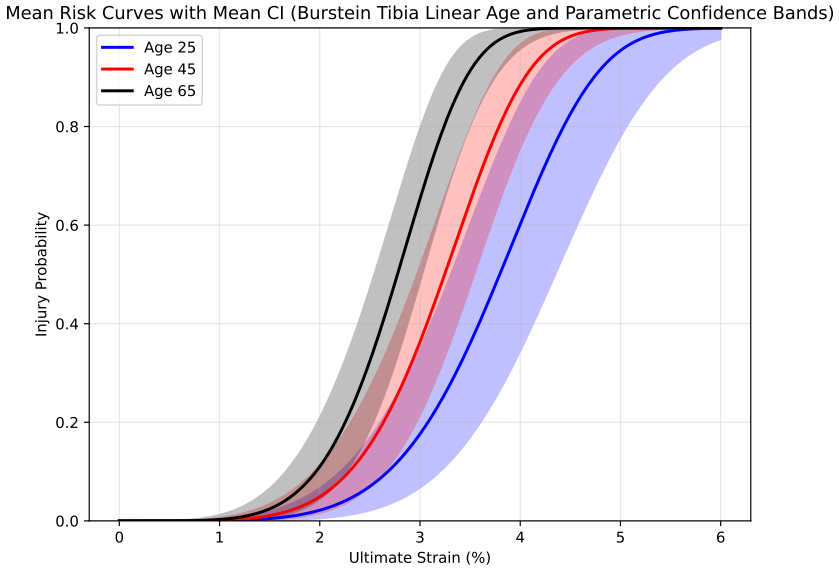

Figure 4.7: Final Tibia fracture injury risk curves developed using Burstein datasets.

4.1.3 Final Weibull Model Parameters

The final Weibull model parameters obtained from the survival analysis are summarized in tables 4.1 and 4.2 for the femur and tibia respectively.
For the femur, the shape parameter decreases from the McCalden dataset to the combined dataset, reflecting the broader spread of failure strains introduced by combining the two data sources. The scale parameter of the combined dataset lies between those of the two individual datasets, consistent with the averaging effect of merging specimens from both sources. The negative age effect coefficient across all three femur datasets confirms that fracture probability at a given strain level increases with age across all formulations, with the combined dataset producing an intermediate age effect between the McCalden and Burstein individual estimates.

Table 4.1: Final Weibull model parameters for femur injury risk functions followed by the Final Weibull Model function for the combined dataset.

Dataset	β	λ_0	β_1	Age (%)
McCalden et al.	4.25	5.20	-0.013	12.19
Burstein et al.	5.29	4.25	-0.00629	6.09
Combined Dataset	4.13	4.78	-0.01	9.52

$$P(\epsilon|\text{Age}) = 1 - \exp\left[-\left(\frac{\epsilon}{4.78e^{-0.01\cdot\text{Age}}}\right)^{4.13}\right] \tag{4.1}$$

Note: β is the Weibull shape parameter, λ_0 is the scale parameter, and β_1 is the age coefficient. Age (%) represents the percentage change in characteristic fracture tolerance per decade of age, calculated as $100[\exp(10\beta_1) - 1]$ [16].

For the Tibia, the shape parameter of 5.43 is higher than that of a femur combined

dataset. The scale parameter of 4.94 places the 50% fracture probability at a higher strain level than observed for the femur combined dataset. The age coefficient of -0.007825 is smaller in magnitude compared to femur combined dataset indicating a weaker age effect in tibia injury risk function.

Table 4.2: Final Weibull model parameters for tibia injury risk functions followed by the final Weibull model function for the Burstein dataset.

Dataset	β	λ_0	β_1	Age (%)
Burstein et al.	5.43	4.94	-0.00783	7.53

$$P(\epsilon|\text{Age}) = 1 - \exp\left[-\left(\frac{\epsilon}{4.94e^{-0.00783\cdot\text{Age}}}\right)^{5.43}\right] \tag{4.2}$$

Note: β is the Weibull shape parameter, λ_0 is the scale parameter, and β_1 is the age coefficient. Age (%) represents the percentage change in characteristic fracture tolerance per decade of age, calculated as $100[\exp(10\beta_1) - 1]$ [16].

4.2 Finite Element Validation Results

4.2.1 Femur 3-point Bending Simulation Correlation

The finite element femur bending simulations were compared against the experimental results reported by Ivarsson et al. across all ten specimens. Validation focused on global structural response using internal force and impactor displacement histories as the primary quantities. Since the simulations were displacement-controlled, force-time histories were extracted and plotted alongside the experimental traces for each specimen. Agreement was assessed by comparing peak force magnitude, which corresponded to the point of maximum displacement at fracture initiation.
A comparison between the experimental and simulated force-time histories for one of the femur specimen is shown in figure 4.8. The simulation reproduced the overall structural response well, including the loading slope, peak force magnitude and the displacement at which the sudden force drop associated with fracture timing. Good agreement between simulation and experiment was observed consistently across the full set of eight femur specimen, as can be seen in appendix A.1.

4.2.2 Tibia 4-point Bending Simulation Correlation

The finite element tibia simulations were compared against the four point bending experiments reported by Harden et al. across all ten specimen. A comparison for specimen Tib007 is shown in figure 4.9, which shows good agreement between the predicted and experimental force time histories in terms of both peak force magnitude and the shape of the loading curve for this specimen.
However, the agreement across the full specimen set was more variable than for the femur, as can be seen in appendix B.1. Approximately half of the tibia specimens showed reasonable agreement in both peak force magnitude and curve shape, while the remaining specimens exhibited deviations in both the peak force level and the

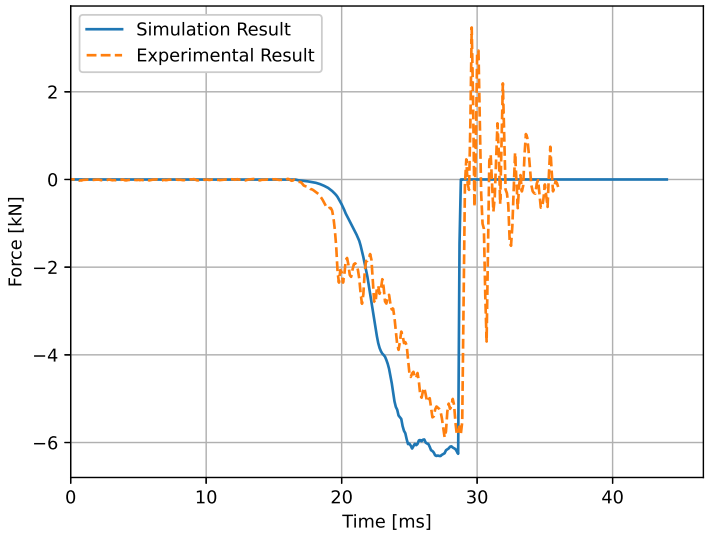

Figure 4.8: Comparison between experimental and simulated force-time response for femur 3-point bending. Specimen: 390R (Age: 63)

force evolution in time. These deviations are further discussed in Chapter 5, but are considered to reflect the sensitivity of the tibia loading configuration to specimen specific geometries and variability which was not capture fully by morphing procedure applied in present work.

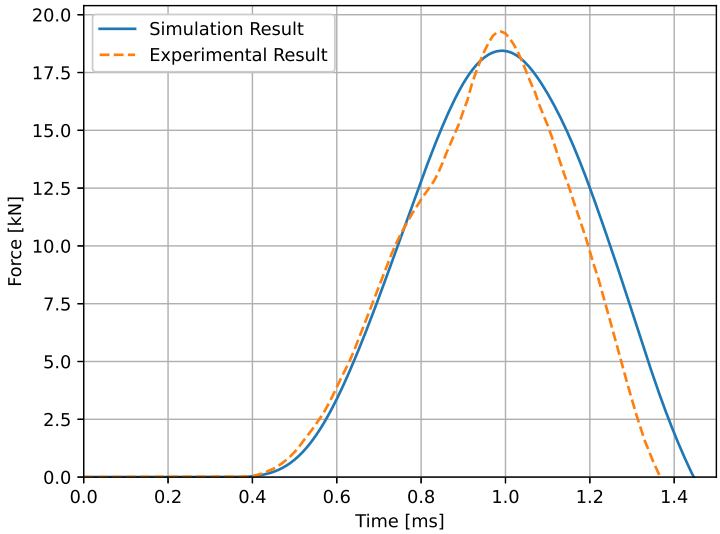

Figure 4.9: Comparison between experimental and simulated force-time response for tibia 4-point bending. Specimen: Tib007 (Age: 73)

4.2.3 Cortical Strain Time Histories

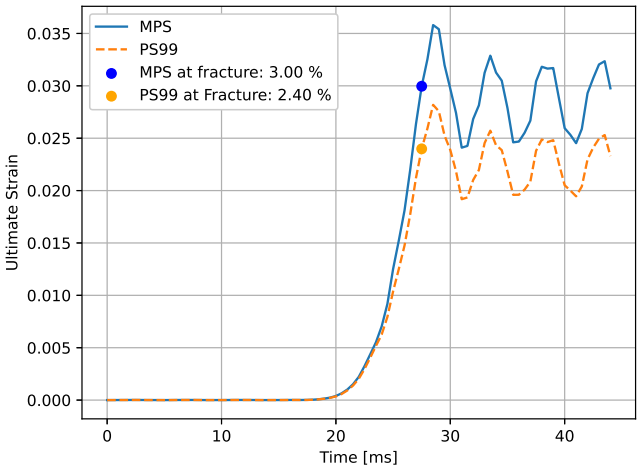

Figure 4.10: Cortical bone strain time history for femur three-point bending. Specimen: 390R (Age: 63)

In addition to the force time validation, cortical bone strain time histories were extracted from the simulations for both the femur and tibia from the outer membrane as mentioned in section 3.2.3.2, forming the basis for the validation of subsequent injury risk function.
For the femur, the peak maximum principal strain and 99th percentile strain were tracked throughout the loading duration. The strain at the time of fracture was identified as the value corresponding to the sudden drop in impactor force, which coincides with the arrest of impactor displacement in the simulation. Representative strain time histories for the femur specimens are shown in figure 4.10.

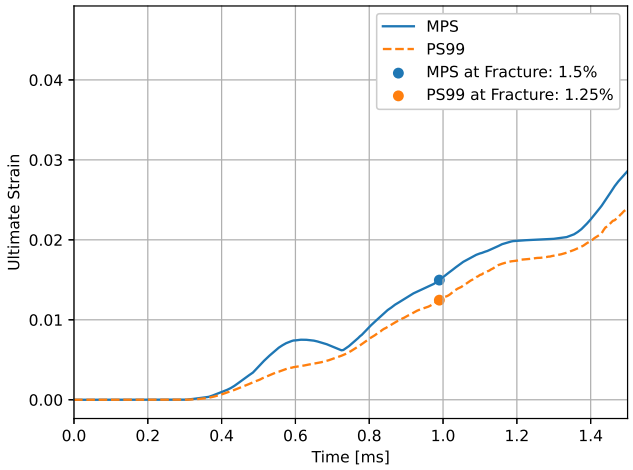

Figure 4.11: Cortical bone strain time history for tibia four-point bending. Specimen: Tib007 (Age: 73)

For the tibia, strain time histories were similarly extracted throughout the loading duration. Since the exact time of fracture could not be determined from the available experimental data, as neither impactor displacement nor a clear force drop indicative of fracture was identifiable across the specimen, the maximum principal strain at the time of experimental peak force was adopted as the representative fracture strain for injury risk evaluation. This assumption is discussed further is Chapter 5. Representative strain time histories for the tibia specimens are shown in figure 4.11 Across all femur and tibia specimens, the peak element strain and 99th percentile element strain tracked closely throughout the loading duration, with no cases of significant divergence between two measures. This confirms that peak strain value extracted from the simulation are not dominated by numerical artifacts and can be considered physically representative of the cortical strain state in the critical region.

4.3 Strain-Based Injury Risk Evaluation

The maximum principal strain values extracted from the cortical bone simulations were evaluated using the developed probabilistic injury risk functions to estimate fracture probability for each specimen.

4.3.1 Femur Injury Prediction Results

The extracted peak strain values and corresponding fracture risk predictions for the femur specimens are summarized in table 4.3. The fracture risk was evaluated using the combined dataset injury function at the age corresponding to each specimen. The predicted fracture risk exceeded 50% for the four of the femur specimens, consistent with the experimentally observed fracture outcome in all cases. The predicted risk increased with increasing cortical strain and specimen age, in agreement with the age dependent Weibull formulation.

Specimen	Age	Exp (kN)	Sim (kN)	Peak Strain (%)	Injury Risk(%)
362R	51	-5.01	-5.67	1.90	16.9
386R	52	-2.38	-2.04	0.36	0.02
390R	63	-5.88	-6.31	3.00	86.39
391L	62	-5.37	-4.69	4.22	99.96
391R	62	-6.47	-6.02	4.43	99.99
392L	45	-3.50	-4.44	0.81	0.42
392R	45	-5.57	-5.07	3.78	91.41
394L	57	-2.91	-3.70	1.69	13.41

Table 4.3: Femur results including strain and injury risk

4.3.2 Tibia Injury Prediction Results

The extracted strain values and corresponding fracture risk predictions for the tibia specimens are summarized in table 4.4. The fracture risk was evaluated using the

Burstein tibia injury risk function at the age of each specimen, with strain extracted at the time of peak experimental force as described in Section 4.2.3.
In contrast to the femur results, the predicted fracture risk remained below 50% across all tibia specimens, with values falling predominantly in the range of 0-10%. Since all experimental tibia specimen did fracture, this indicates that the developed FE validation framework was not able to validate the IRF in the same manner as the femur. The strain values extracted across specimens were clustered within a relatively narrow range, suggesting that the variability in predicted fracture risk was limited and that the current FE framework may be underestimating the true tissue level strain at fracture for the tibia loading configuration. The possible reasons for this outcome are examined in detail in the next chapter

Table 4.4: Tibia simulation results and predicted fracture risks.

Specimen	Age	Exp (kN)	Sim (kN)	Fracture Strain (%)	Injury Risk (%)
Tib001	64	12.7	14.81	1.15	0.55
Tib002	63	20.2	16.11	1.28	0.95
Tib003	77	16.6	16.06	0.9	0.26
Tib004	84	17.2	19.01	1.42	4.00
Tib005	86	15.4	17.03	1.31	2.83
Tib006	102	12.5	16.99	1.34	6.21
Tib007	73	19.3	18.44	1.5	3.39
Tib008	74	16.7	16.17	1.47	3.17
Tib009	85	18.6	17.82	1.61	8.10
Tib010	89	21.9	18.31	1.06	1.03

5

Discussion

This thesis set out to develop and validate strain-based fracture injury risk functions for the femur and tibia within the SAFER HBM framework, addressing a gap in the pedestrian injury assessment capabilities of the model. The work produced age-dependent probabilistic IRFs for both bones grounded in cortical bone coupon test data, implemented a component-level finite element validation framework using whole bone bending experiments, and demonstrated the feasibility of translating local cortical strain outputs from FE simulation into quantitative fracture probability estimates. The femur IRF showed encouraging partial validation, with four out of eight specimens correctly predicted to fracture above the 50% probability threshold and consistent force-time agreement across the full specimen set. The tibia validation, while inconclusive in terms of fracture risk prediction, revealed important insights into the limitations of the experimental setup and the challenges of validating IRFs under highly dynamic direct-contact loading conditions. The discussion that follows interprets these outcomes in detail, examines the factors contributing to the observed discrepancies, and contextualizes the limitations of the present work within the broader goal of establishing a robust pedestrian injury assessment framework for the SAFER HBM.

5.1 Injury Risk Functions

5.1.1 Age Effect Comparison Between Datasets in Femur IRF

The age effect observed in the femur injury risk functions differed notably between the two data sources. Using the methodology described by Kalbfleisch [16], the age effect was calculated to be approximately 12.1% reduction in fracture strain per decade for the McCalden dataset, compared to 6.1% per decade calculated for the Burstein dataset. This difference is visually captured in figure 4.4, where McCalden curves show a more pronounced leftward shift with increasing age compared to the Burstein curves, particularly for the 45 and 65 year age group.

Several factors may contribute to this discrepency. McCalden explicitly states in his paper that the experimental setup and loading rate were designed to match those used by Burstein, meaning the difference is unlikely stem from methodological incompatibility between the two studies.

A natural question arising from this discrepency is why the two datasets were combined for the femur IRF despite the difference in observed age effect. The answer

lies not in resolving the disagreement between the datasets, but in the practical necessity of maximizing the available sample size for probabilistic modeling. With 33 PMHS in the Burstein dataset and 46 in the McCalden dataset, Combining the two datasets increases the effective sample size to 79 specimens per Monte Carlo realization, reducing the width of the confidence bands and producing a more stable Weibull fit as seen in figure 4.5. Their combination produces an intermediate age effect that may better represent the true population average than either dataset alone.

5.1.2 Monte Carlo Variability and Justification

The Monte Carlo reconstruction produced tightly clustered injury risk curve across all 500 realizations for both femur and tibia Burstein dataset, as visible in figure 4.2 and 4.6. This clustering persisted even when the number of realizations was increased beyond 1000, confirming that the tight spread is a fundamental property of the reconstruction rather than an artifact of insufficient sampling.
This behavior is a direct consequence of the constraints imposed by the reconstruction methodology and the rather large sample size. Since each dataset is generated by sampling from a normal distribution defined strictly by the reported mean and standard deviation, the resulting dataset are tightly constrained to reproduce the same summary statistics across realization. The reconstruction therefore does not generate edge cases because sampling constraints prevent synthetic specimens from deviating far from reported group means.
The decision to proceed with the Monte Carlo framework rather than fitting a single Weibull model directly to the reported group means was deliberate. Working with synthetic individual-level data, even tightly constrained, allows the survival analysis to be performed in a statistically rigorous manner that accounts for the continuous age covariate and produces parametric confidence intervals through the flexsurv framework. The Monte Carlo approach also provides a transparent representation of the uncertainty associated with the reconstruction, even if that uncertainty is ultimately small given the constraints of the available data.

5.1.3 Limitations of Tibia IRF

A fundamental limitation of the tibia IRF compared to the femur is the reliance on a single aggregated data source. While the femur IRF benefitted from the combination of two datasets no equivalent individual-level tibia cortical bone dataset was available in the literature for the present work. The tibia IRF therefore rests entirely on the reconstructed Burstein data, which as discussed in section 5.1.2 produces tightly constrained Monte Carlo realizations with limited variability. The consequence for this is the modest age effect inherited from the Burstein data may underestimate the true age dependency of the cortical bone fracture, as suggested by the stronger age effect observed in the McCalden femur data.
Improving the tibia injury risk function would therefore require access to individual-level cortical bone coupon test data from tibia specimens spanning a broad age range, ideally reported with specimen-level age and failure strain measurements

comparable to what McCalden provided for the femur. Such data would allow a more robust and statistically independent tibia IRF to be developed, reducing reliance on the aggregated Burstein statistics and providing a stronger foundation for future validation efforts. Despite these limitations, the developed tibia injury risk function represents a reasonable first estimate based on the best available data, and is considered sufficient for use within the SAFER HBM framework as a starting point for pedestrian injury assessment pending the availability of more comprehensive tibia-specific experimental data.

5.2 Finite Element Model Validation

5.2.1 Femur and Tibia Finite Element Models

The femur and tibia finite element models were developed by extracting and morphing the corresponding bone geometries from the SAFER HBM, with the cortical and trabecular regions retained from the original model. Both models used 8-node fully integrated hexahedral solid elements throughout the cortical and trabecular bone regions, consistent with the element formulation defined in the original SAFER HBM. The femur model contained approximately 25,000 cortical bone elements and the tibia model approximately 14,000 elements.
To enable extraction of maximum principal strain at the outer cortical surface a thin membrane of 0.1 mm thickness was applied to the outer surface of the cortical bone region in both models. The membrane was assigned the same material properties as the underlying cortical bone solid elements. Maximum principal strain values used for injury risk evaluation were extracted from this membrane layer throughout the simulation duration.

5.2.2 Femur Validation

The femur finite element model predictions showed good agreement with the experimental force-time histories reported by Ivarsson et al. across all 8 specimens. Both the loading shape and peak force magnitude were well reproduced between simulation and experiment for majority of cases. The consistent agreement across all the specimen provides confidence in the morphed femur geometry and the chosen material parameters. The fact that good force-time correlation was achievable despite the absence of CT scan data and the geometric simplifications inherent in the morphing procedure suggests that the four geometric parameters targeted during morphing i.e., total length, lateral-medial diameter, posterior-anterior diameter, and cortical cross-sectional area, are sufficient to capture the dominant determinants of bending stiffness in the femoral shaft under three-point bending conditions.

5.2.3 Tibia Validation

In contrast to the femur, the tibia simulations showed considerably more variable agreement with the experimental results reported by Harden et al. Approximately half of the ten specimens showed reasonable agreement in both peak force magnitude

and force-time curve shape, while the remaining specimens exhibited notable deviations in both quantities. Some hypotheses are proposed to explain this discrepancy which are supported to varying degrees by available evidence.
The most significant distinguishing feature of the Harden experimental setup compared to the Ivarsson femur configuration is the combination of high impact velocity and the absence of any foam pad between the impactor and the bone surface. At 6 m/s with direct cortical contact, the inertia of the entire experimental system contributes significantly to the measured force response, rather than the force reflecting only the structural resistance of the bone. The foam pad in the femur setup would have dampened this effect, but the primary driver is the high impact velocity itself. This manifests as an excitation of the natural frequency of the tibia-fixture system during impact which is evident in several specimens where the experimental force-time curves exhibit a nearly sinusoidal character around the peak, with an upward trend in force observable toward the end of the 2 ms recording window as seen in Figure 4 in Harden et al. (2021) [11]. Under these conditions, the recorded peak force reflects the dynamic response of the entire system governed by loading magnitude, system mass and damping characteristics, rather than the structural resistance of the bone alone. This has direct implications for the fracture timing assumption adopted in the present work. If the peak force is primarily a manifestation of the system eigenfrequency rather than the point of maximum bone deformation, then using it as a proxy for fracture introduces additional uncertainty into the strain extraction process.

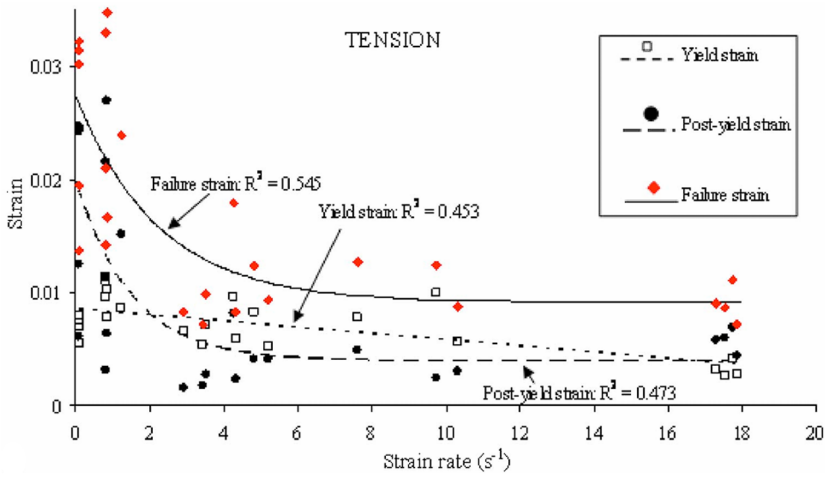

Figure 5.1: Effect of strain rate on tensile strain properties [10]

A second hypothesis concerns the possibility of a strain rate effect on cortical bone fracture behavior. Under the highly dynamic loading conditions of the Harden experiment, where the impact occurs over approximately 2 ms without any energy-absorbing pad, the bone is subjected to strain rates substantially higher than those encountered in the femur experiment. Research by Hansen et al. [10] has demonstrated that cortical bone mechanical properties are strain rate dependent, with increased stiffness and altered failure characteristics at higher loading rates as seen in figure 5.1. While strain rate effects were not incorporated into the material model

used in the present work they may contribute to the observed discrepancy between simulated and experimental structural response in the tibia case.
Finally, the load cell representation in the finite element model requires a brief discussion as well. The load cell was modeled as a stiff block, and its Young's modulus was tuned to reduce the frequency of force oscillations from approximately 15 oscillations per millisecond to approximately 1 oscillation per millisecond, bringing it into closer alignment with the measurement frequency of the experimental load cells. This tuning had a minor effect on the recorded force magnitude within the first oscillation, with values remaining in a similar range to the untuned model, and is therefore not considered a significant source of error in the force-time comparison.

5.3 Strain Based Injury Risk Evaluation

5.3.1 Femur

The strain based injury risk evaluation produced fracture probability predictions above 50% for half of the femur specimen when evaluated against the combined dataset IRF. Since the IRF is a mean estimation of the populations tolerance to injury risk, it is quite difficult to have an accurate IRF that predicts fracture all the time. This is due to the wide band of fracture strains within a given population set. The good performance of the femur IRF is the result of two factors working in combination. First, the force-time agreement between simulation and experiment was strong across the specimen set, meaning that the cortical strain values extracted at the time of fracture are likely representative of the true tissue level deformation at the time of fracture. Second, the combined femur injury risk function benefits from a larger effective sample size and broader population representation than either individual dataset alone, producing a more robust probabilistic model that generalizes better across the age range of the experimental specimens.

5.3.2 Tibia

The tibia injury risk evaluation was unable to validate the developed IRF in the same manner as the femur. The maximum principal strains extracted at the time corresponding to peak experimental force were clustered within a narrow range of approximately 1% to 1.7% across all ten specimens which well below the strain level at which tibia IRF predicts 50% fracture probability.
The narrow clustering of extracted strains across specimens with different ages and geometric dimensions suggests that the strain values are not driven by specimen-specific biological variability, but rather by the loading conditions and the fracture timing assumption itself. By fixing the strain extraction to the time of peak experimental force and assuming a constant impactor velocity to map this time onto the simulation, the extracted strain values are strongly constrained by the loading configuration rather than reflecting the true variability in fracture tolerance across the specimen set.
This outcome does not necessarily indicate that the tibia injury risk function is incorrect. Rather, it reflects the difficulty of extracting a meaningful fracture strain

from the current experimental setup and simulation framework. The combination of direct impactor contact, high impact velocity, uncertain fracture timing, and variable force-time agreement across specimens introduces a level of uncertainty in the strain extraction process that prevents a definitive validation conclusion from being drawn. Establishing a reliable tibia IRF validation would require experimental data with clearer fracture timing information as well as a loading configuration that more closely resembles the femur validation setup used in the present work, where the presence of a foam pad between the impactor and the bone surface moderated the loading rate and distributed the contact force more physiologically, allowing the FE model to capture the structural response with greater fidelity.

6

Conclusion

This thesis addressed the development and validation of strain-based fracture injury risk functions for the femoral and tibial shafts, with the aim of extending the pedestrian injury assessment capabilities of the SAFER HBM. The work was guided by two primary objectives: the development of age-dependent probabilistic IRFs from cortical bone coupon test data, and the validation of these functions through component-level finite element simulations of whole bone bending experiments.

The first objective was fully achieved for both bones. Age dependent Weibull injury risk functions were successfully developed for the femur and tibia using cortical bone coupon test data from Burstein et al. and McCalden et al. For the femur, the combination of individual-level McCalden data with the statistically reconstructed Burstein data produced a robust probabilistic IRF with reduced uncertainty compared to either dataset alone. The Monte Carlo framework ensured that the uncertainty associated with working from aggregated experimental data was transparently represented in the final curves. For the tibia, the IRF was developed solely from the reconstructed Burstein data and, despite the limitations of relying on a single aggregated source, represents a reasonable first estimate suitable for use within the SAFER HBM framework pending the availability of more comprehensive tibia-specific experimental data.

The second objective was partially achieved. The femur finite element simulations showed consistently good force-time agreement with the experimental results reported by Ivarsson et al. across all eight specimens, and the developed IRF predicted fracture probability above 50% for four of the eight specimens. The tibia validation was inconclusive. Although force-time agreement was achieved for approximately half of the ten specimens, the maximum principal strains extracted at the time of peak experimental force were clustered in the range of 1% to 1.7% across all specimens. A critical limitation of the tibia validation is that the exact time of fracture initiation in the Harden experiments is unknown. As seen in Figure 4.11, the cortical strain in the tibia simulations is still increasing steeply at the assumed fracture time, meaning the extracted strain is highly sensitive to this assumption. So, a shift of even a fraction of a millisecond in the assumed fracture time would produce substantially different strain values and consequently very different fracture probability predictions. This uncertainty in fracture timing, combined with the highly dynamic nature of the Harden experimental setup where direct impactor contact at 6 m/s introduces inertial effects and potential eigenfrequency excitation of the tibia-fixture system, means that the extracted strain values cannot be considered reliable inputs to the IRF under the current framework.

Overall, the present work establishes a strain-based injury assessment framework

for the femur and tibia, grounded in probabilistic survival analysis and component-level finite element validation. The femur IRF is considered validated for use in pedestrian injury assessment, while the tibia IRF, though not yet validated, provides a meaningful first estimate that can be refined as better experimental data and validation setups become available.

6.1 Future Work

Several directions are identified for extending and improving upon the work presented in this thesis.

Improved tibia experimental validation. The most immediate priority is the identification of a more suitable experimental dataset for tibia IRF validation. The ideal setup would incorporate a soft tissue surrogate between the impactor and the bone surface to moderate the loading rate and distribute contact forces more physiologically, as was the case in the femur validation experiment. Clear fracture timing information would additionally allow the cortical strain to be extracted at the true moment of fracture rather than at an assumed time point, substantially improving the reliability of the validation outcome.

Integration into full-body pedestrian simulation. The validated IRFs developed in this thesis are intended for use within the SAFER HBM in full-body pedestrian impact simulations. A natural next step is to use the femur and tibia IRFs directly together with the SAFER HBM and conduct pedestrian-to-vehicle impact simulations under representative crash conditions. The predicted fracture probabilities extracted from these simulations could then be compared against injury outcome data from real-world pedestrian accidents or controlled PMHS experiments, providing a population-level validation of the integrated framework and enabling assessment of vehicle safety systems with respect to lower extremity fracture risk.

Tibia-specific cortical bone coupon data. The tibia IRF currently relies entirely on the aggregated Burstein dataset, which limits both the statistical robustness of the function and the confidence in its age dependency. Obtaining individual-level cortical bone coupon test data from tibia specimens spanning a broad age range, comparable to the McCalden dataset available for the femur, would allow a substantially more robust tibia IRF to be developed. While such data are not currently available in the literature, future experimental campaigns targeting tibia-specific fracture properties would represent a significant contribution to the field.

CT scan based geometric morphing. The morphing procedure used in the present work targeted only four global geometric parameters due to the absence of CT scan data for the experimental specimens. Access to specimen-specific CT scans for future validation studies would enable cortical thickness distribution, cross-sectional shape, and local geometric features to be reproduced with significantly greater accuracy, reducing the geometric uncertainty in the extracted cortical strain values and potentially improving both force-time agreement and fracture risk predictions.

Bibliography

[1] J. G. Betts et al. *Anatomy and Physiology 2e*. OpenStax, 2022. URL: https://openstax.org/details/books/anatomy-and-physiology-2e/.

[2] A. Blennow. "Improvement of Human Body Model Rib Fracture Risk Prediction: Creation of Injury Risk Curves and Rib Cortical Bone Regression Models for Age Adjusted Risk Prediction". Master's thesis. Chalmers University of Technology, 2020. URL: https://odr.chalmers.se/server/api/core/bitstreams/1aec59fc-942b-4d6b-a840-c2d2b60880b2/content.

[3] A.H. Burstein et al. "Contribution of collagen and mineral to the elastic-plastic properties of bone". In: *Journal of Bone and Joint Surgery* 57A (1976), pp. 956–961. DOI: 10.2106/00004623-197557070-00013.

[4] D.R. Carter and D.M. Spengler. "Mechanical properties and composition of cortical bone". In: *Clinical Orthopaedics and Related Research* 135 (1978), pp. 192–217. URL: https://pubmed.ncbi.nlm.nih.gov/361320/.

[5] M. Ceddia et al. "Stress Analysis of Tibial Bone Using Three Different Materials for Bone Fixation Plates". In: *Journal of Composites Science* 8.9 (2024), p. 334. DOI: 10.3390/jcs8090334.

[6] P.C. Dischinger et al. "Consequences and Costs of Lower Extremity Injuries". In: *Annual Proceedings of the Association for the Advancement of Automotive Medicine* 48 (2004), pp. 339–353. URL: https://pmc.ncbi.nlm.nih.gov/articles/PMC3217424/.

[7] R. L. Drake et al. *Gray's Anatomy for Students*. 3rd. Churchill Livingstone/Elsevier, 2015. ISBN: 978-0-7020-5131-9.

[8] J. L. Forman et al. "Whole-body Response for Pedestrian Impact with a Generic Sedan Buck". In: *Stapp Car Crash Journal* 59 (2015), pp. 401–444. DOI: 10.4271/2015-22-0016.

[9] J.L. Forman et al. "Predicting rib fracture risk with whole-body finite element models: Development and preliminary evaluation of a probabilistic analytical framework". In: *Annals of Advances in Automotive Medicine* (2012). URL: https://pmc.ncbi.nlm.nih.gov/articles/PMC3503420/.

[10] U. Hansen et al. "The Effect of Strain Rate on the Mechanical Properties of Human Cortical Bone". In: *Journal of Biomechanical Engineering* 130.1 (2008), p. 011011. DOI: 10.1115/1.2838032.

[11] A.L. Harden et al. "Preliminary Sex-specific Relationships between Peak Force and Cortical Bone Morphometrics in Human Tibiae Subjected to Lateral Loading". In: *Proceedings of the International Research Council on the Biomechanics of Injury (IRCOBI)*. 2021. URL: www.researchgate.net/publication/355479429.

[12] J. Iraeus et al. *Development of SAFER HBM v11*. Tech. rep. 2024:06. Chalmers University of Technology, 2024. DOI: 10.5281/zenodo.10886711.

[13] J. Iraeus and B. Pipkorn. "Development and Validation of a Generic Finite Element Ribcage to be used for Strain-based Fracture Prediction". In: *Proceedings of the International Research Council on the Biomechanics of Injury (IRCOBI)*. Florence, Italy, 2019, pp. 193–210. URL: https://www.ircobi.org/wordpress/downloads/irc19/pdf-files/35.pdf.

[14] B.J. Ivarsson et al. "The Tolerance of the Femoral Shaft in Combined Axial Compression and Bending Loading". In: *Stapp Car Crash Journal, Vol. 53* (2009), pp. 251–290. DOI: 10.4271/2009-22-0010.

[15] C. H. Jackson. "flexsurv: A Platform for Parametric Survival Modeling in R". In: *Journal of Statistical Software* 70.8 (2016), pp. 1–33. DOI: 10.18637/jss.v070.i08.

[16] J. D. Kalbfleisch and R. L. Prentice. *The Statistical Analysis of Failure Time Data*. 2nd. John Wiley & Sons, 2002. ISBN: 0-471-36357-X.

[17] M.J. Katzenberger et al. "Effects of sex, age, and two loading rates on the tensile material properties of human rib cortical bone". In: *Journal of the Mechanical Behavior of Biomedical Materials* 102 (2020). DOI: 10.1016/j.jmbbm.2019.103489.

[18] A.R. Kemper et al. "Material Properties of Human Rib Cortical Bone from Dynamic Tension Coupon Testing". In: *Stapp Car Crash Journal* 49 (2005), pp. 199–230. DOI: 10.4271/2005-22-0010.

[19] A.R. Kemper et al. "The Biomechanics of Human Ribs: Material and Structural Properties from Dynamic Tension and Bending Tests". In: *Stapp Car Crash Journal* 51 (2007), pp. 235–273. DOI: 10.4271/2007-22-0011.

[20] J.R. Kerrigan et al. "Experiments for Establishing Pedestrian-Impact Lower Limb Injury Criteria". In: *SAE Technical Paper* 2003-01-0895 (2003). DOI: 10.4271/2003-01-0895.

[21] D.G. Kleinbaum and M. Klein. *Survival Analysis: A Self-Learning Text*. Springer, 2005. DOI: 10.1007/978-1-4419-6646-9.

[22] K. D. Klinich and L. W. Schneider. *Biomechanics of Pedestrian Injuries Related to Lower Extremity Injury Assessment Tools: A Review of the Literature and Analysis of Pedestrian Crash Database*. Tech. rep. UMTRI-2003-25. University of Michigan Transportation Research Institute (UMTRI), 2003. URL: https://deepblue.lib.umich.edu/bitstream/2027.42/1535/2/97318.0001.001.pdf.

[23] Jennifer Lange et al. *General Human Anatomy*. LibreTexts, 2023. URL: https://med.libretexts.org/Bookshelves/Anatomy_and_Physiology/Human_Anatomy_(Lange_et_al.).

[24] Karl-Johan Larsson et al. "Rib Cortical Bone Fracture Risk as a Function of Age and Rib Strain: Updated Injury Prediction Using Finite Element Human Body Models". In: *Frontiers in Bioengineering and Biotechnology* 9 (2021), p. 677768. DOI: 10.3389/fbioe.2021.677768.

[25] N. Lindgren et al. "Development of Personalizable Female and Male Pedestrian SAFER Human Body Models". In: *Traffic Injury Prevention* 25.2 (2024), pp. 182–193. DOI: 10.1080/15389588.2023.2281280.

[26] R.W. McCalden et al. “Age-related changes in the tensile properties of cortical bone. The relative importance of collagen content and pore size”. In: *Journal of Bone and Joint Surgery* 75A (1993), pp. 1428–1436. DOI: 10.2106/00004623-199308000-00009.

[27] D. Mikulić et al. “Protection of Pedestrians from Collisions With Motor Vehicles”. In: *Journal of Traffic and Transport Theory and Practice* 9.2 (2024), pp. 90–100. DOI: 10.7251/JTTTP2402090M.

[28] E.F. Morgan, G.U. Unnikrisnan, and A.I. Hussein. “Bone mechanical properties in healthy and diseased states”. In: *Annual Review of Biomedical Engineering* 20 (2018), pp. 119–143. DOI: 10.1146/annurev-bioeng-062117-121139.

[29] R. Paas, C. Masson, and J. Davidsson. “Head Boundary Conditions in Pedestrian Crashes with Passenger Cars: Six-Degrees-of-Freedom Post-Mortem Human Subject Responses”. In: *International Journal of Crashworthiness* 20.6 (2015), pp. 547–559. DOI: 10.1080/13588265.2015.1060731.

[30] A. Petitjean et al. “Injury risk curves for the WorldSID 50th male dummy”. In: *Stapp Car Crash Journal* 56 (2012). DOI: 10.4271/2009-22-0016.

[31] B. Pipkorn et al. “Multi-Scale Validation of a Rib Fracture Prediction Method for Human Body Models”. In: *Proceedings of the International Research Council on the Biomechanics of Injury (IRCOBI)*. Florence, Italy, 2019. URL: https://research.chalmers.se/publication/517644/file/517644_Fulltext.pdf.

[32] B. Pipkorn et al. “Validation of the SAFER Human Body Model Kinematics in Far-Side Impacts”. In: *Proceedings of the International Research Council on the Biomechanics of Injury (IRCOBI)*. 2021, pp. 444–476. URL: https://research.chalmers.se/publication/529443/file/529443_Fulltext.pdf.

[33] C.B. Ruff and W.C. Hayes. “Sex Differences in Age-Related Remodeling of the Femur and Tibia”. In: *Journal of Orthopaedic Research* 6.6 (1988), pp. 886–896. DOI: 10.1002/jor.1100060613.

[34] A. Schubert et al. “Development of a 50th Percentile Female Femur Model”. In: *Proceedings of the International Research Council on the Biomechanics of Injury (IRCOBI)*. 2021, pp. 308–332. URL: https://www.ircobi.org/wordpress/downloads/irc21/pdf-files/2138.pdf.

[35] C. Simms and D. Wood. “Pedestrian and Cyclist Impact: A Biomechanical Perspective”. In: *Solid Mechanics and its Application* (2009). DOI: 10.1007/978-90-481-2743-6_2.

[36] Y. Takahashi et al. “Development and validation of a finite element model for the human lower limb of pedestrians”. In: *Stapp Car Crash Journal* 44 (2000), pp. 163–178. DOI: 10.4271/2000-01-SC22.

[37] E. Weissenbacher. “Prediction of Lower Extremity Injuries in Pedestrian Accidents”. Master’s thesis. Graz University of Technology, 2022. DOI: 10.3217/197t4-pmn79.

[38] World Health Organization. *Global Status Report on Road Safety 2023*. Tech. rep. World Health Organization, 2023. URL: https://www.who.int/teams/

social-determinants-of-health/safety-and-mobility/global-status-report-on-road-safety-2023.

[39] T. Xu et al. “Development and Validation of Dummies and Human Models Used in Crash Test”. In: *Applied Bionics and Biomechanics* 2018 (2018), p. 3832850. DOI: 10.1155/2018/3832850.

[40] J. Yang. “Review of Injury Biomechanics in Car-Pedestrian Collisions”. In: *International Journal of Vehicle Safety* 1.1/2/3 (2005), pp. 100–117. DOI: 10.1504/IJVS.2005.007540.

A

Appendix A

This appendix presents the complete set of FE simulation results for the Femur three-point bending cases. Force-time comparisons between simulation and experiment are provided for all eight specimen in section A.1, supplementing the representative example shown in figure 4.8 in results. Cortical strain time histories showing peak maximum principal strain and 99th percentile element strain are provided for all eight speciemn in section A.2.

A.1 Femur Force-Time Histories

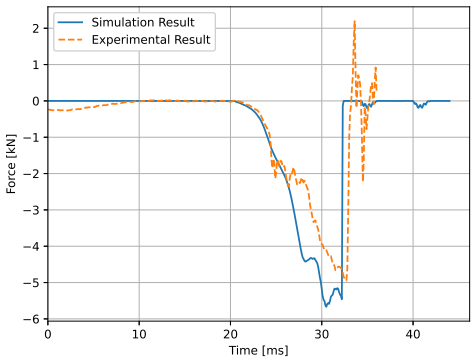

Figure A.1: Specimen: 362R (Age: 51)

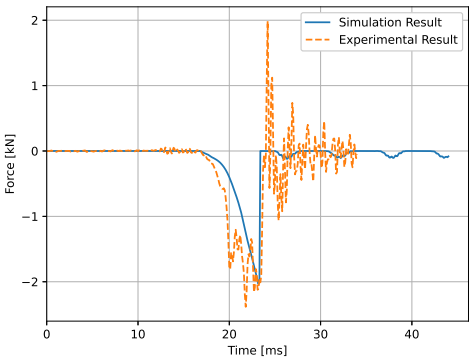

Figure A.2: Specimen: 386R (Age: 52)

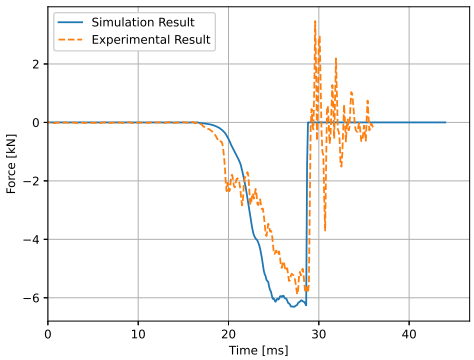

Figure A.3: Specimen: 390R (Age: 63)

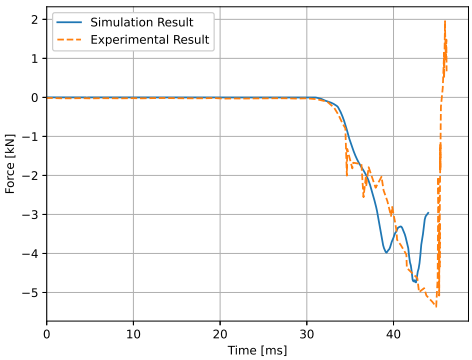

Figure A.4: Specimen: 391L (Age: 62)

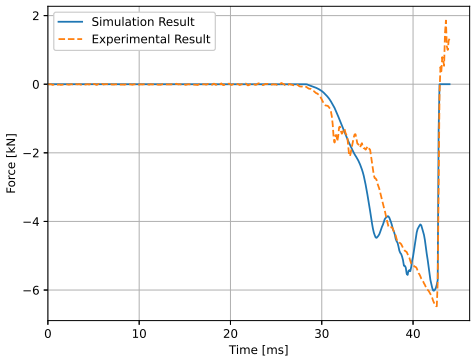

Figure A.5: Specimen: 391R (Age: 62)

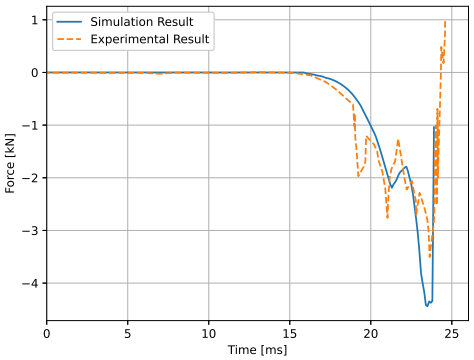

Figure A.6: Specimen: 392L (Age: 45)

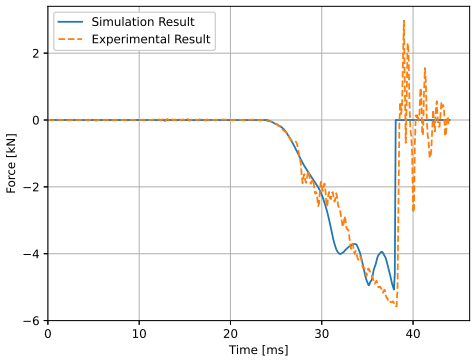

Figure A.7: Specimen: 392R (Age: 45)

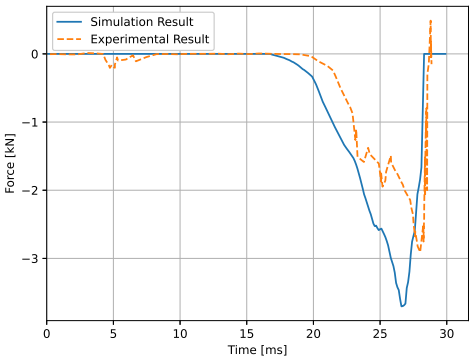

Figure A.8: Specimen: 394L (Age: 57)

A.2 Femur Cortical Strain Time Histories

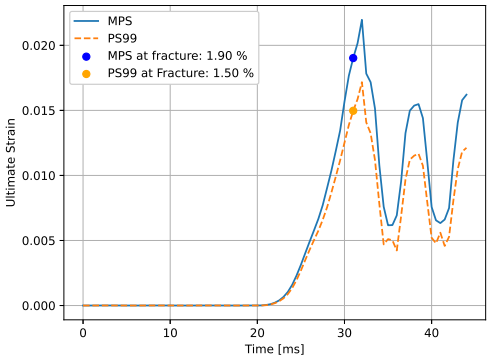

Figure A.9: Specimen: 362R (Age: 51)

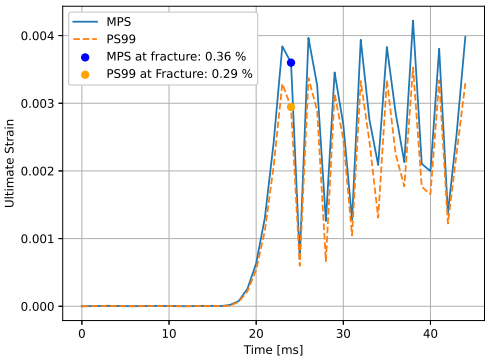

Figure A.10: Specimen: 386R (Age: 52)

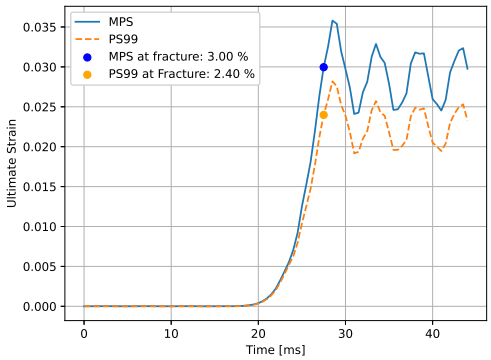

Figure A.11: Specimen: 390R (Age: 63)

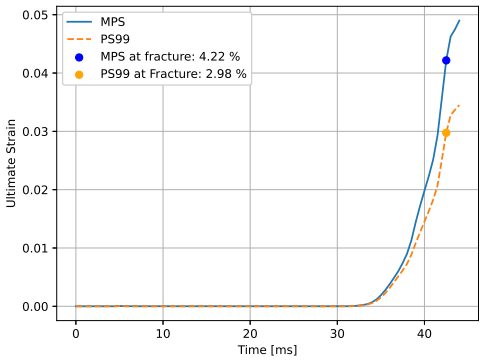

Figure A.12: Specimen: 391L (Age: 62)

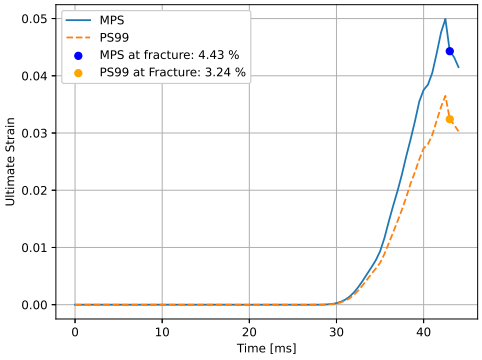

Figure A.13: Specimen: 391R (Age: 62)

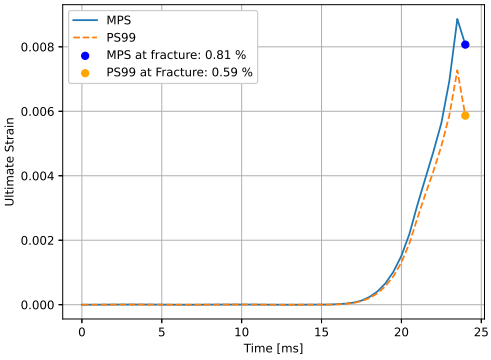

Figure A.14: Specimen: 392L (Age: 45)

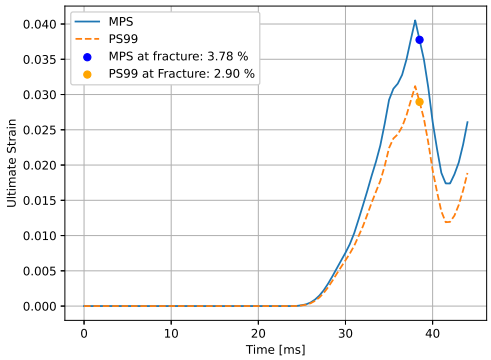

Figure A.15: Specimen: 392R (Age: 45)

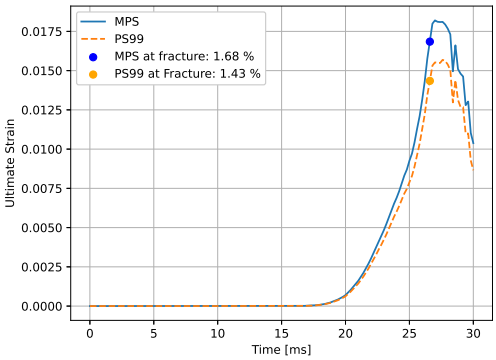

Figure A.16: Specimen: 394L (Age: 57)

B

Appendix B

This appendix presents the complete set of FE simulation results for the Tibia four-point bending cases. Force-time comparisons between simulation and experiment are provided for all ten specimen in section B.1, supplementing the representative example shown in figure 4.9 in results. Cortical strain time histories showing peak maximum principal strain and 99th percentile element strain are provided for all eight speciemn in section B.2.

B.1 Tibia Force-Time Histories

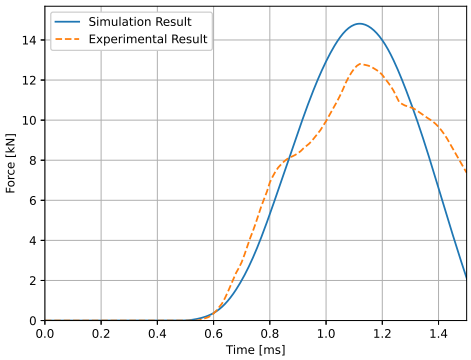

Figure B.1: Specimen: Tib001 (Age: 64)

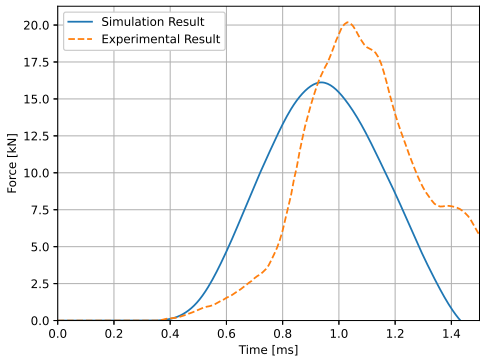

Figure B.2: Specimen: Tib002 (Age: 63)

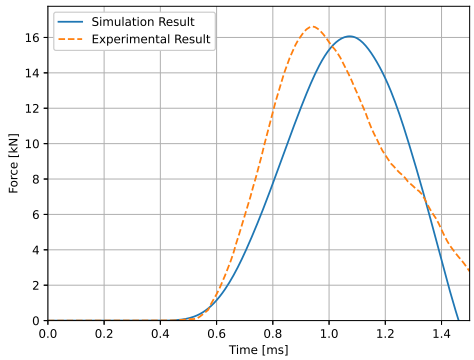

Figure B.3: Specimen: Tib003 (Age: 77)

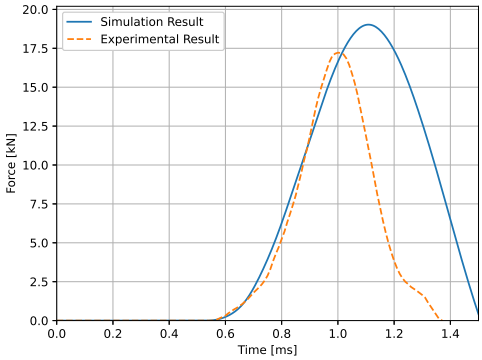

Figure B.4: Specimen: Tib004 (Age: 84)

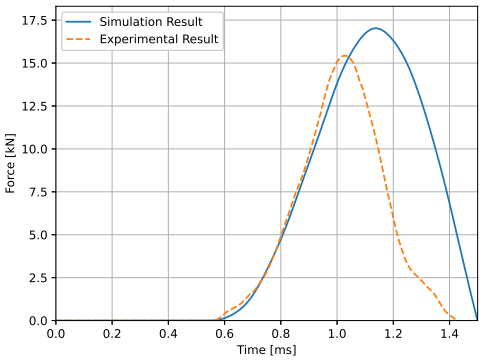

Figure B.5: Specimen: Tib005 (Age: 86)

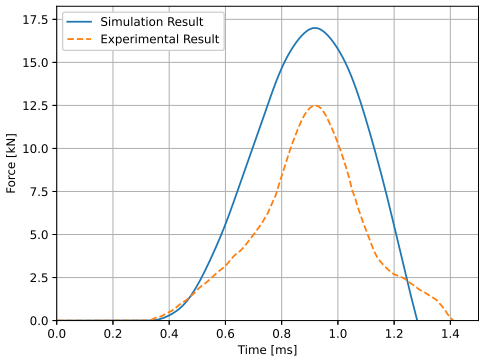

Figure B.6: Specimen: Tib006 (Age: 102)

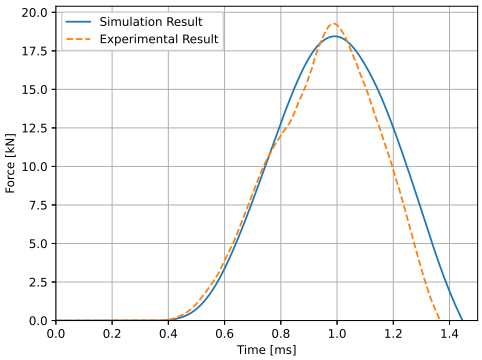

Figure B.7: Specimen: Tib007 (Age: 73)

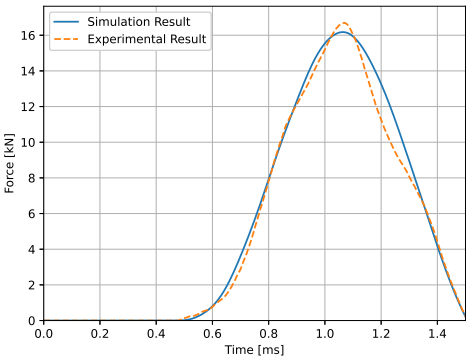

Figure B.8: Specimen: Tib008 (Age: 74)

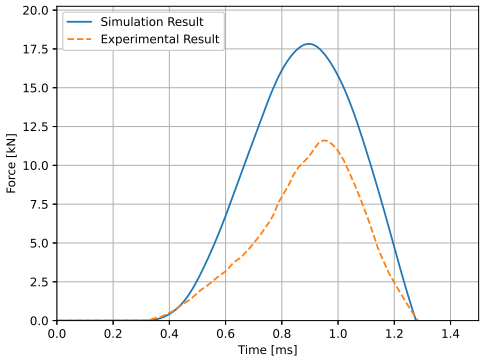

Figure B.9: Specimen: Tib009 (Age: 85)

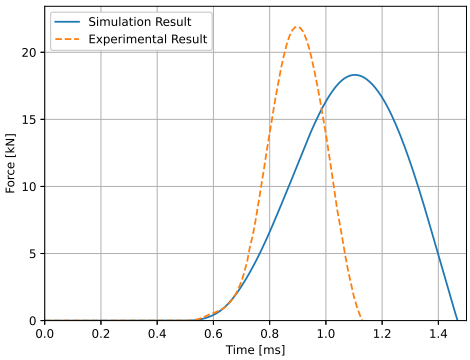

Figure B.10: Specimen: Tib010 (Age: 89)

B.2 Tibia Cortical Strain Time Histories

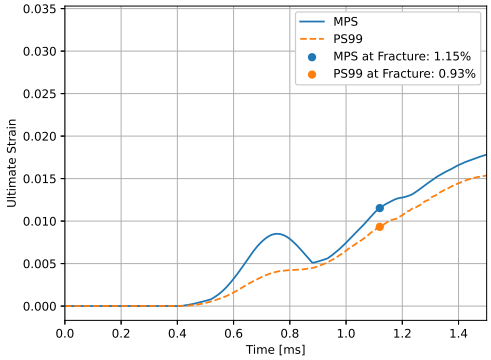

Figure B.11: Specimen: Tib001 (Age: 64)

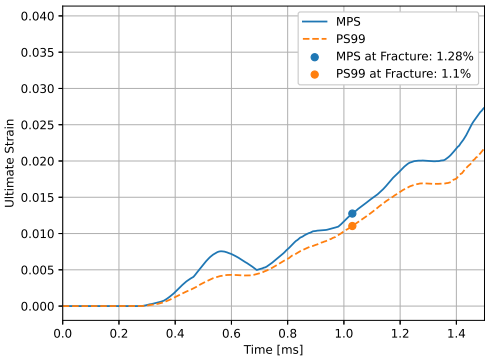

Figure B.12: Specimen: Tib002 (Age: 63)

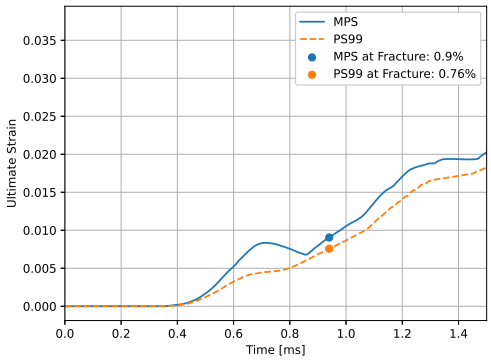

Figure B.13: Specimen: Tib003 (Age: 77)

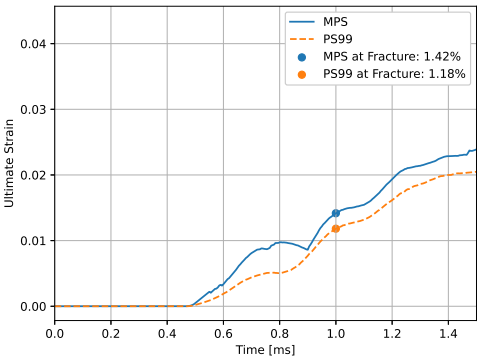

Figure B.14: Specimen: Tib004 (Age: 84)

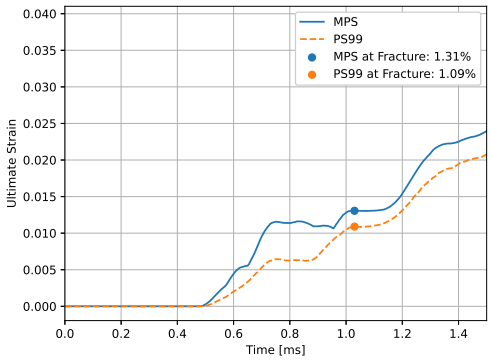

Figure B.15: Specimen: Tib005 (Age: 86)

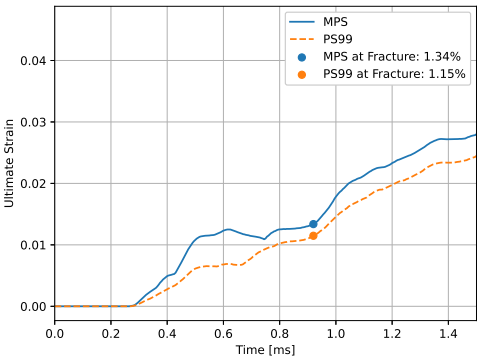

Figure B.16: Specimen: Tib006 (Age: 102)

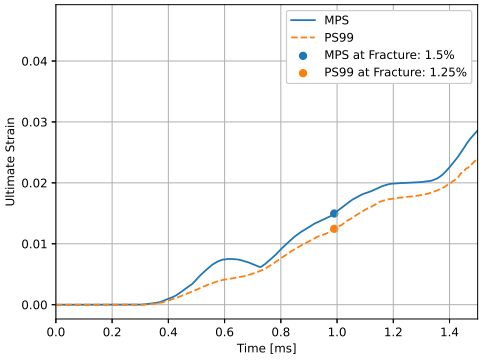

Figure B.17: Specimen: Tib007 (Age: 73)

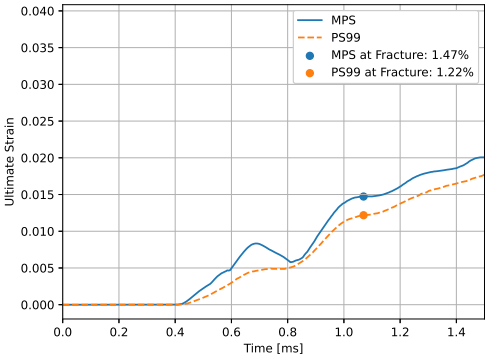

Figure B.18: Specimen: Tib008 (Age: 74)

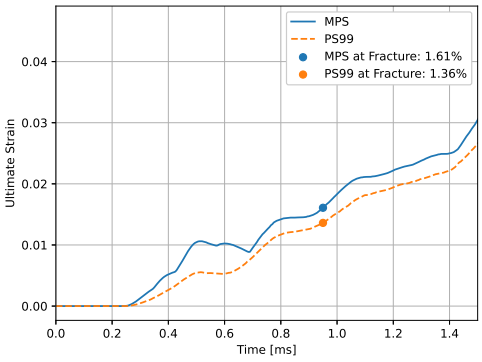

Figure B.19: Specimen: Tib009 (Age: 85)

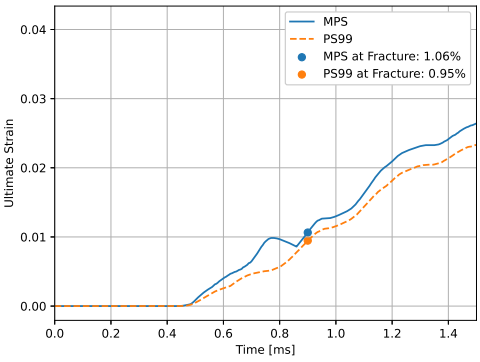

Figure B.20: Specimen: Tib010 (Age: 89)

C

Appendix C

This appendix provides the technical details required for a reader to correctly apply the injury risk functions developed in this thesis within a finite element simulation using the SAFER HBM or a compatible cortical bone model.

C.1 C.1 Valid Region for Fracture Prediction

The injury risk functions developed in this thesis are valid for fracture prediction in the diaphyseal region of the femur and tibia only. Specifically, the functions apply to the middle third of each bone, defined as the region between 33% and 67% of total bone length measured from the distal end. The proximal third (67–100% from distal) and distal third (0–33% from distal) are outside the scope of these risk functions, as the experimental coupon data used to derive them were sourced from the mid-diaphysis and the whole-bone validation experiments loaded the mid-shaft region. Applying the IRFs to epiphyseal or metaphyseal regions would constitute an extrapolation beyond the validated domain and is not recommended.

C.2 C.2 Outer Skin Membrane Definition in LS-DYNA

To enable accurate extraction of maximum principal strain at the outer cortical surface, a thin shell membrane was applied to the external surface of the cortical bone solid mesh in both the femur and tibia models. In ANSA, this outer skin was created as a surface mesh coincident with the outer cortical boundary.

Element formulation **ELFORM = 5** (Belytschko–Tsay membrane element) was used. This formulation carries in-plane loads only and has no bending stiffness, meaning the membrane does not contribute additional flexural stiffness to the underlying solid mesh. The shell thickness was set to **0.1 mm**, which is negligible relative to cortical wall thickness (typically 3–8 mm in the mid-shaft) and was verified to have no measurable effect on the global force-time response or local strain distribution of the cortical bone solid elements.

The membrane was assigned the same material card as the underlying cortical bone solid elements (`MAT_PIECEWISE_LINEAR_PLASTICITY`, MAT024) with identical elastic modulus, yield stress, and hardening curve. Cards C.1–C.2–C.3 give the complete LS-DYNA keyword input for both bones and the outer skin section.

```
*MAT_PIECEWISE_LINEAR_PLASTICITY_TITLE
Burstein_Cortical_Femur
$#      MID           RO            E           PR
    1900064        2.E-6         17.7          0.3
$#     SIGY         ETAN         FAIL         TDEL
      0.121            1.        1.E20           0.
$#       C1           C2          LC1          LC2
          0.           0.
$#   EPS(1)       EPS(2)       EPS(3)       EPS(4)
          0.           0.           0.           0.
          0.           0.           0.           0.
```

Card C.1: MAT024 card for femur cortical bone (Burstein 1976). Unit system: mm, tonne, s (stress in MPa, density in t/mm^3).

```
*MAT_PIECEWISE_LINEAR_PLASTICITY_TITLE
Tibia_Cortical_Burstein_1976
$#      MID           RO            E           PR
     900052        2.E-6         28.8          0.3
$#     SIGY         ETAN         FAIL         TDEL
       0.14         1.39        1.E20           0.
$#       C1           C2          LC1          LC2
          0.           0.           0            0
$#   EPS(1)       EPS(2)       EPS(3)       EPS(4)
          0.           0.           0.           0.
          0.           0.           0.           0.
```

Card C.2: MAT024 card for tibia cortical bone (Burstein 1976). Fields and units as per Card C.1.

```
*SECTION_SHELL_TITLE
Outer_Skin
$#    SECID       ELFORM         SHRF          NIP
   10000042            5                        2.
$#    PROPT      QR/IRID        ICOMP        SETYP
          1.            0            0
$#       T1           T2           T3           T4
         0.1          0.1          0.1          0.1
$#     NLOC        MAREA         IDOF       EDGSET
                                    0.
```

Card C.3: Section card for the outer skin shell membrane. ELFORM = 5 (Belytschko–Tsay membrane, in-plane loads only, no bending stiffness). Thickness T = 0.1 mm at all four integration points.

C.3 C.3 Strain Extraction Procedure

The injury metric used with the risk functions is the **maximum principal strain (first principal strain, ε_1)** extracted from the outer skin membrane elements. The procedure is as follows:

1. At each output time step, the first principal strain is computed for every element in the outer skin membrane part.
2. Two scalar values are recorded per time step:
   - **MPS** — the single peak element value across all membrane elements (maximum of the distribution).
   - **PS99** — the 99th percentile element value across all membrane elements, used to confirm that the MPS is not dominated by a numerically isolated artefact such as a distorted element near a boundary condition or contact interface.
3. Close agreement between MPS and PS99 throughout the loading history indicates that the peak strain field is physically representative and not driven by numerical noise. In the present work, MPS and PS99 tracked within approximately 20–25% of each other across all specimens, confirming the validity of the extracted values.
4. The strain value entered into the injury risk function (Equations 4.1 and 4.2) is the **MPS at the time of fracture**. For applications where the time of fracture corresponds to a sudden drop in impactor force, the MPS at that instant should be used. Where fracture timing is unavailable, the MPS at peak force may be used as a conservative estimate, subject to the assumptions discussed in Section 4.2.3.

Strain extraction should be restricted to membrane elements located within the valid diaphyseal region defined in Section C.1. Elements in the potted end regions should be excluded to avoid boundary-condition artefacts.

DEPARTMENT OF MECHANICS AND MARITIME SCIENCE
CHALMERS UNIVERSITY OF TECHNOLOGY
Gothenburg, Sweden
www.chalmers.se

CHALMERS
UNIVERSITY OF TECHNOLOGY